

Dependencies of Simulated Convective Cell and System Growth Biases on Atmospheric Instability and Model Resolution

Zhixiao Zhang¹, Adam Varble², Zhe Feng³, James Marquis⁴, Joseph Clinton Hardin³, and Edward J. Zipser⁵

¹University of Oxford

²Pacific Northwest National Laboratory

³Pacific Northwest National Laboratory (DOE)

⁴Unknown

⁵Department of Atmospheric Sciences, University of Utah, Salt Lake City, Utah, USA

March 13, 2024

Abstract

This study evaluates convective cell properties and their relationships with convective and stratiform rainfall within a season-long convection-permitting simulation over central Argentina using measurements from the RELAMPAGO-CACTI field campaign. While the simulation reproduces the total observed rainfall, it underestimates stratiform rainfall by 46% and overestimates convective rainfall by 43%. As Convective Available Potential Energy (CAPE) increases, the overestimation of convective rainfall decreases, but the underestimation of stratiform rainfall increases such that the high bias in the contribution of convective rainfall to total rainfall remains approximately constant at 26% across all CAPE conditions. Overestimated convective rainfall arises from the simulation generating 2.6 times more convective cells than observed despite similar observed and simulated cell growth processes, with relatively wide cells contributing most to excessive convective rainfall. Relatively shallow cells, typically reaching heights of 4–7 km, contribute most to the cell number bias. This bias increases as CAPE decreases, potentially because cells and their updrafts become narrower and more under-resolved as CAPE decreases. The gross overproduction of shallow cells leads to overly efficient precipitation and inadequate detrainment of ice aloft, thereby diminishing the formation of robust stratiform rainfall regions. Decreasing the model's horizontal grid spacing from 3 to 1 or 0.333 km for representative low and high CAPE cases results in minimal change to the cell number and depth biases, while the stratiform and convective rainfall biases also fail to improve. This suggests that improving prediction of deep convective system growth depends on factors beyond solely increasing model resolution.

Hosted file

Zhang et al 2024 JGR Submission Final 2.docx available at <https://authorea.com/users/750905/articles/722026-dependencies-of-simulated-convective-cell-and-system-growth-biases-on-atmospheric-instability-and-model-resolution>

Hosted file

Zhang et al 2024 JGR Submission Supplemental Final.docx available at <https://authorea.com/users/750905/articles/722026-dependencies-of-simulated-convective-cell-and-system-growth-biases-on-atmospheric-instability-and-model-resolution>

1
2 **Dependencies of Simulated Convective Cell and System Growth Biases on**
3 **Atmospheric Instability and Model Resolution**

4 **Zhixiao Zhang^{1†}, Adam C. Varble^{1,2}, Zhe Feng², James N. Marquis², Joseph C. Hardin²,**
5 **and Edward J. Zipser¹**

6 ¹Department of Atmospheric Sciences, University of Utah, Salt Lake City, Utah, USA

7 ²Atmospheric, Climate, and Earth Sciences Division, Pacific Northwest National Laboratory,
8 Richland, Washington, USA

9 Corresponding author: Adam C. Varble (adam.varble@pnnl.gov)

10 † Current Affiliation: Department of Physics, University of Oxford, Oxford, England, UK

11 **Key Points:**

- 12 • A convection-permitting simulation overestimates the convective contribution to total
13 rainfall, while underestimating stratiform rainfall.
- 14 • A large excess of simulated shallow convective cells increases as instability decreases,
15 contributing to the stratiform rainfall bias.
- 16 • Increasing model resolution does not improve convective cell and convective-stratiform
17 rainfall partitioning biases.

18 Abstract

19 This study evaluates convective cell properties and their relationships with convective and
20 stratiform rainfall within a season-long convection-permitting simulation over central Argentina
21 using measurements from the RELAMPAGO-CACTI field campaign. While the simulation
22 reproduces the total observed rainfall, it underestimates stratiform rainfall by 46% and
23 overestimates convective rainfall by 43%. As Convective Available Potential Energy (CAPE)
24 increases, the overestimation of convective rainfall decreases, but the underestimation of
25 stratiform rainfall increases such that the high bias in the contribution of convective rainfall to
26 total rainfall remains approximately constant at 26% across all CAPE conditions. Overestimated
27 convective rainfall arises from the simulation generating 2.6 times more convective cells than
28 observed despite similar observed and simulated cell growth processes, with relatively wide cells
29 contributing most to excessive convective rainfall. Relatively shallow cells, typically reaching
30 heights of 4–7 km, contribute most to the cell number bias. This bias increases as CAPE
31 decreases, potentially because cells and their updrafts become narrower and more under-resolved
32 as CAPE decreases. The gross overproduction of shallow cells may lead to inadequate
33 detrainment of ice aloft, thereby diminishing the formation of robust stratiform rainfall regions.
34 Decreasing the model's horizontal grid spacing from 3 to 1 or 0.333 km for representative low
35 and high CAPE cases results in minimal change to the cell number and depth biases, while the
36 stratiform and convective rainfall biases also fail to improve. This suggests that improving
37 prediction of deep convective system growth depends on factors beyond solely increasing model
38 resolution.

39 Plain Language Summary

40 The ability of a storm-resolving weather model to predict rainfall over central Argentina was
41 evaluated with data from a field campaign. Although the model accurately predicted the total
42 amount of rain, it produced far too much relatively heavy rainfall and not enough light rainfall.
43 The overestimation of intense rainfall increased as the atmosphere became less favorable for
44 intense storms, which correlated with far too many predicted storm cells, especially ones that
45 were relatively shallow. The excessive frequency of storm cells prevented the formation of
46 widespread lighter rainfall that was much more frequent in observations. Increasing the spatial
47 resolution of the model to better resolve storm circulations did not improve predictions,
48 suggesting model representation of storm precipitation formation and growth processes requires
49 improvement beyond model resolution to better predict storm rainfall intensities.

50 1 Introduction

51 Organized convective clouds critically impact weather (e.g., extreme precipitation and
52 severe winds) and climate (e.g., synoptic waves, intra-seasonal to seasonal oscillations, and
53 decadal teleconnections) through redistributing atmospheric heat, moisture, and momentum
54 (Houze, 2004). Convective regions correspond to net latent heating at nearly all heights, while
55 stratiform regions correspond to net heating in the upper troposphere and net cooling in the lower
56 troposphere (e.g., Schumacher et al., 2004; Liu et al., 2015) with a dependence on the height of
57 condensate transport from convective regions (Han et al., 2019). Relatively greater stratiform
58 contributions to total latent heating integrated in time and space elevates tropical large-scale
59 circulation responses and wave propagation from the tropics to extratropics (e.g., Schumacher et
60 al., 2004). Accurate representation of convective-stratiform partitioning by area and precipitation

61 as a function of system life cycle and ambient environmental conditions is crucial for weather
62 and climate prediction.

63 Weather and climate models have difficulties reproducing observed convective-stratiform
64 partitioning. General circulation models (GCMs) used for long-range climate prediction and
65 global weather models are too coarse to resolve convective-scale processes such that convection
66 parameterizations are needed. However, most sub-grid scale convection parameterizations do not
67 attempt to represent stratiform regions or mesoscale organization. Stratiform precipitation is left
68 to grid scale processes (e.g., Pan & Randall, 1998) or parameterized by semi-empirical relations
69 (e.g., Donner, 1993; Donner et al., 2001; Yang et al., 2013). Higher resolution convection-
70 permitting models (CPMs) with usually 4 km or less horizontal grid spacing explicitly allow
71 convection, can resolve mesoscale circulations, and are often able to reproduce observed rainfall
72 totals (e.g., Prein et al., 2013). Nevertheless, CPMs often fail to reproduce observed convective-
73 stratiform area and rainfall partitioning, underestimating the areal coverage and volume of
74 stratiform precipitation while overestimating the areal coverage and volume of convective
75 rainfall (e.g., Varble et al., 2011, 2014a-b; Caine et al., 2013; Hagos et al., 2014; Fan et al., 2017;
76 Feng et al., 2018, 2023b; Zhang et al., 2021).

77 Model convective cell biases likely contribute to convective-stratiform partitioning
78 biases. Atmospheric circulation boundaries (e.g., fronts, dry lines, terrain flows, boundary layer
79 rolls, cold pool outflows) spatially aggregate convective cells with modulation by vertical wind
80 shear (e.g., Rotunno et al., 1988; Mulholland et al., 2018). Larger and aggregated convective
81 cells have reduced evaporation associated with dry air entrainment (e.g., Jeevanjee & Zhou,
82 2022) and convective updraft merging (Glenn & Krueger, 2017) that may impact precipitation
83 efficiency. These processes may have biased representation in CPMs. Past model evaluations
84 suggest that CPMs overproduce the number of deep convective cores containing heavy rainfall
85 (Yun et al., 2020) while reproducing the number and total rainfall of MCSs (Prein et al., 2017;
86 Zhang et al., 2021). CPMs with kilometer-scale grid spacing also underestimate dry air
87 entrainment (e.g., Bryan & Morrison, 2012) and produce overly wide convective updrafts and
88 downdrafts (e.g., Varble et al., 2020).

89 Convective updrafts horizontally detrains heat, moisture, momentum, and condensate to
90 promote stratiform anvil growth (Houze, 2004). Mesoscale updrafts and downdrafts associated
91 with mid-level inflow in a sheared environment can promote stratiform rainfall enhancement
92 (e.g., Chen & Frank, 1993), but condensate transport is still the primary source for stratiform
93 growth (Gamache & Houze, 1983). Under-resolved and overly wide and strong convective
94 updrafts in km-scale models with excessive riming (e.g., Varble et al., 2014a; Fan et al., 2017;
95 Stanford et al., 2017) may produce insufficient ice detrainment to stratiform regions which limits
96 stratiform precipitation (Varble et al., 2014b; Han et al., 2019). Thus, CPM-overestimated
97 convective contribution to rainfall might stem from coupled dynamical and microphysical
98 processes.

99 The sensitivity of simulated convective cells and updrafts to model resolution has been
100 investigated in many previous case studies using idealized and real case simulations (e.g., Petch
101 et al., 2002; Bryan et al., 2003; Craig & Dörnbrack, 2008; Lebo & Morrison, 2015; Stanford et
102 al., 2020; Wang et al., 2022). Bryan & Morrison (2012) found that convective rainfall and cell
103 depth in a mid-latitude, continental squall line decreased as horizontal grid spacing decreased
104 from 4 km to 250 m, partially because convective updrafts entrained more mid-tropospheric dry
105 air as resolution increased, though such changes are not systematic across all environments (e.g.,

106 Bryan et al., 2003; Morrison et al., 2015). Others have found that convective cell area decreases
107 and convective cell number increases moving from 3-km to finer grid spacing with lesser
108 changes for grid spacing below 200-250 m (Lebo & Morrison, 2015; Nicol et al., 2015; Stanford
109 et al., 2024). Convective updraft strength increases moving from 4-km to 1-km grid spacing
110 owing to decreasing vertical pressure gradient forces as updraft width decreases (Stein et al.,
111 2015; Morrison, 2016). Further decreases in grid spacing to 250-m or less can result in weaker
112 updrafts owing to increasing buoyancy dilution from dry air entrainment effects (e.g., Wang et
113 al., 2020). These convective draft differences can also modulate vertical transport of zonal
114 momentum that affects the convective system's evolution (Varble et al., 2020).

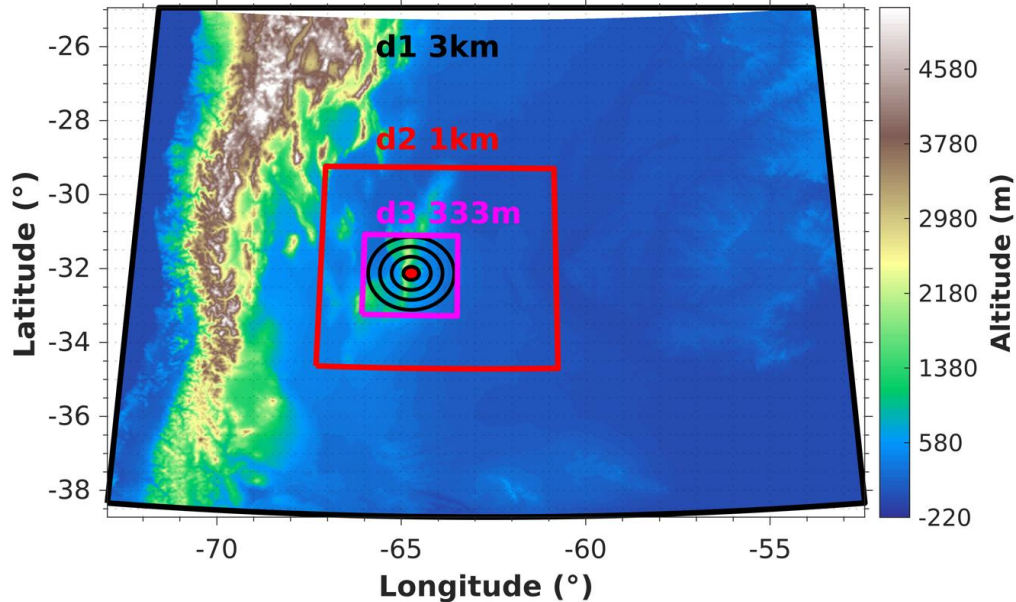
115 With regional weather and climate models already being run with 3–4 km grid spacing
116 (e.g., Casaretto et al., 2021; Dowell et al., 2022), there is an urgent need to understand CPM
117 biases and their causes to guide model improvement. This study leverages a warm season CPM
118 simulation, several case-focused simulations with grid spacing varying from 3 to 0.333 km, and
119 measurements collected from the Remote sensing of Electrification, Lightning, And
120 Mesoscale/microscale Processes with Adaptive Ground Observations (RELAMPAGO; Nesbitt et
121 al., 2021) and Clouds, Aerosols, and Complex Terrain Interactions (CACTI; Varble et al., 2021)
122 field campaigns. A primary objective is to use convective cell tracks to evaluate simulated
123 convective cell growth including its contribution to convective and stratiform precipitation, as
124 well as its sensitivity to convective instability and model resolution.

125 The remaining sections are organized as follows: Section 2 introduces the model setup,
126 observed and simulated datasets, and methods for identifying and tracking convective and
127 stratiform objects. Section 3 presents evaluation of domain-total convective and stratiform
128 rainfall and their interactions. Section 4 analyzes simulated convective cell biases. Section 5
129 investigates convective updraft property contributions to cell biases. Section 6 focuses on the
130 sensitivity of cell biases to model resolution. Finally, discussion and conclusions are presented in
131 Section 7.

132 **2 Data and Methodology**

133 **2.1 Observations**

134 Our analyses focus on the Sierras de Córdoba (SDC) range (the mountain range cutting
135 through d2 and d3 in Figure 1) in central Argentina, which is offset ~400 km east of the Andes.
136 This region is moistened by the northerly South American low-level jet (Salio et al., 2002, 2007;
137 Sasaki et al., 2022, 2024; Vera et al., 2006) under the influence of synoptic troughs (Piersante et
138 al., 2021; Rocque & Rasmussen, 2022) and a surface low pressure in the lee of the Andes
139 (Seluchi et al., 2003) that build convective instability beneath inversions and steep lapse rates
140 caused by westerly flow over the Andes (Rasmussen & Houze, 2011, 2016; Ribeiro & Bosart,
141 2018; Schumacher et al., 2021). This meteorological setup interacts with the mountainous terrain
142 to produce frequent deep convection initiation (Nelson et al., 2021, 2022; Marquis et al., 2021,
143 2023), rapid growth (Mulholland et al., 2018; Feng et al., 2022), and organization (Mulholland et
144 al., 2019; Trapp et al., 2020; Singh et al., 2022) of deep convection, making it a prime location to
145 study deep convective cloud processes. This led to the RELAMPAGO (Nesbitt et al. 2021) and
146 CACTI (Varble et al. 2021) field campaigns being conducted in this area between October 2018
147 and April 2019.



148
149 **Figure 1.** Model domains for conducting the multiscale simulations. The red dot represents the
150 radar and radiosonde location with 20-, 50-, 80-, and 110-km radar range rings in black.

151 About 20 km east of the primary SDC north-south ridgeline, a ground-based C-Band
152 Scanning Atmospheric Radiation Measurement (ARM) Precipitation Radar (CSAPR2) was
153 operated. From October 2018 through February 2019 (Varble et al., 2021), the CSAPR2
154 collected plan projection indicator (PPI) volume scans every 15 minutes with elevation varying
155 from 0.5° and 33° (Hardin et al., 2018). CSAPR2 did not collect PPI volumes from 27 December
156 2018 to 20 January 2019, 9 February to 23 February 2019, and after 3 March 2019 due to
157 operational interruptions. Non-meteorological and second-trip echoes are removed using the
158 Taranis radar processing package (Hardin et al., 2020). Rain rates are retrieved using quality
159 controlled CSAPR2 reflectivity, differential reflectivity, and specific differential phase
160 measurements for points without likely hail contamination, following Bringi & Chandrasekar
161 (2001). These retrievals were then re-gridded to Cartesian coordinates with 500-m horizontal and
162 vertical grid spacing using the Python ARM Radar Toolkit (Helmus & Collis, 2016).

163 The processed CSAPR2 dataset is used to analyze convective-stratiform rainfall
164 partitioning and convective cell life cycles. Every 15-minute Top-Of-Atmosphere (TOA)
165 infrared (IR) brightness temperature (T_b) measurement at 2-km grid spacing (Smith and Thieman
166 2019) from Geostationary Operational Environmental Satellite 16 (GOES-16) is matched to
167 radar-tracked convective cells (see section 2.3 for tracking details). Environmental conditions are
168 derived from the Interpolated Sonde (INTERPSONDE) product (Fairless & Giangrande, 2018).
169 INTERPSONDE temporally interpolates radiosondes with scaling of the moisture profiles to
170 continuous precipitable water measurements collected by a microwave radiometer. Inputted
171 radiosondes were launched every 3 to 4 hours at the CSAPR2 site between 12 and 00 UTC (9–21
172 LT). These sounding derived parameters are matched in time with each convective cell's
173 initiation time.

174 2.2 Simulations

175 A convection-permitting simulation covering 15 October 2018 to 30 April 2019 was
176 conducted using the Weather Research and Forecasting (WRF: Skamarock & Klemp, 2019)

177 model version 4.1.1 with 15-minute output that matches the observed radar volume frequency.
 178 Its domain (d2) is shown in Figure 1. The simulation is performed at 3-km horizontal grid
 179 spacing with 80 vertical levels preferentially stacked below 5-km altitude but with all layer
 180 thicknesses less than 500 m. Microphysical processes are parameterized using the Thompson
 181 aerosol aware scheme (Thompson & Eidhammer, 2014), planetary boundary layer (PBL)
 182 processes are parameterized using the Mellor-Yamada Nakanishi Niino (Nakanishi & Niino,
 183 2006, 2009) eddy diffusivity mass flux scheme, the surface layer is parameterized by the Eta
 184 similarity scheme (Janjic, 2002), and radiation is parameterized by the RRTMG shortwave and
 185 longwave schemes (Iacono et al., 2008). This model setup is very similar to the operational High
 186 Resolution Rapid Refresh (HRRR) model (Dowell et al., 2022). Rainfall is computed at 2.5 km
 187 above mean sea level (AMSL) consistent with observations for comparisons to avoid ground
 188 clutter and variable lowest radar beam heights with range while remaining below the melting
 189 level. Contributions of graupel and hail to precipitation are ignored in simulations to be
 190 consistent with radar retrievals.

191 **Table 1.** Case Study Simulation Time Periods

Simulation	Domains	Analysis Periods	d1 Restart	d2 Initialization	d3 Initialization
Low CAPE 3 km	d1	00–12Z, 26 Nov	12Z, 25 Nov	N/A	N/A
Low CAPE 1 km	d1, d2	00–12Z, 26 Nov	12Z, 25 Nov	12:15Z, 25 Nov	N/A
Low CAPE 333 m	d1, d2, d3	00–12Z, 26 Nov	12Z, 25 Nov	12:15Z, 25 Nov	18:15Z, 25 Nov
High CAPE 3 km	d1	16Z, 10 Nov – 6Z, 11 Nov	12Z, 09 Nov	N/A	N/A
High CAPE 1 km	d1, d2	16Z, 10 Nov – 6Z, 11 Nov	12Z, 09 Nov	4:15Z, 10 Nov	N/A
High CAPE 333 m	d1, d2, d3	16Z, 10 Nov – 6Z, 11 Nov	12Z, 09 Nov	4:15Z, 10 Nov	10:15Z, 10 Nov

192 Higher resolution simulations for two convective cases are conducted with innermost
 193 domain horizontal grid spacings of 1 and 0.333 km, respectively (Fig. 2). As described in Table
 194 1, case study simulations that include the higher resolution domains are run for two separate
 195 periods representing low CAPE conditions ($< 300 \text{ J kg}^{-1}$) and high CAPE conditions ($> 1000 \text{ J}$
 196 kg^{-1}). In each period, there are 3 simulations performed, one with only d1, a second with d2
 197 nested into d1, and a third with d3 nested into d2 and d1. Two-way nesting is employed. These
 198 simulations are restarted from the seasonal simulation using a 12 UTC (9 LT) restart file prior to
 199 the start of the event. The nested inner domains (d2 and d3) are delayed in their starts and
 200 allowed to spin up for 11.75 hours and 5.75 hours, respectively. Exact restart, initiation, and
 201 analysis times are listed in Table 1. The total simulated hours including model spin up are 24
 202 hours for the 3 low CAPE period runs and 30 hours for the 3 high CAPE period runs. The full
 203 CSAPR2 coverage area (110 km range) is encapsulated by d3 (Fig. S1). All 3 domains have the
 204 same vertical levels and physics parameterizations used in the seasonal run, except that the

205 planetary boundary layer scheme is turned off in d3, where diffusion is computed using a
 206 prognostic equation for the 1.5-order turbulent kinetic energy closure (Bretherton & Park, 2009).

207 2.3 Convective Cell Tracking

208 Observed and simulated convective cells are consistently tracked using the open-source
 209 PyFLEXTRKR algorithm (Feng et al., 2023a) applied to 15-minute composite (column
 210 maximum) reflectivity maps derived from the WRF simulations and the CSAPR2 observations.
 211 The melting layer was designed to avoid cell identifications associated with high melting level
 212 reflectivity (Feng et al., 2022). The CSAPR2 reflectivity measurements at native 500-m grid
 213 spacing, and the higher resolution simulations with 0.333-km and 1-km horizontal grid spacing,
 214 are conservatively coarsened to 3-km horizontal grid spacing by averaging reflectivity in linear
 215 units ($\text{mm}^6 \text{m}^{-3}$) and then converting to \log_{10} (dBZ) units. Terrain blockage of CSAPR2 radar
 216 beams is analyzed with a digital elevation map using the wradlib (Heistermann et al., 2013)
 217 Python package. The same beam blockage mask is applied to the WRF output to have consistent
 218 observing volumes with measurements. Dates and times in which the CSAPR2 did not obtain
 219 PPI volumes were also removed in the WRF dataset.

220 Following the method in Steiner et al. (1995), the tracking algorithm identifies convective
 221 cores using the horizontal texture of composite reflectivity by defining the peakedness of each
 222 point, which is the difference between each grid point reflectivity (Z_{grid}) and the surrounding
 223 background reflectivity (Z_{bkg}). Z_{bkg} is defined using averaged values within a 13.5-km radius
 224 from each 3-km spacing grid point. A grid point is classified as a convective core if the
 225 reflectivity peakedness ($Z_{grid} - Z_{bkg}$) is higher than the reflectivity-dependent threshold equal
 226 to $10\cos(\pi Z_{bkg}/120)$ or if Z_{grid} exceeds 55 dBZ. To avoid over-segmentation, identified
 227 convective cores are further expanded with a Z_{bkg} -dependent dilation radius (R_{core}) defined by
 228 Equation 1 where R_{core} has units of km and Z_{bkg} has units of dBZ:

$$R_{core} = \min \left[\max \left(3 + 0.5 \left\lfloor \frac{Z_{bkg} - 25}{5} \right\rfloor, 3 \right), 5 \right] \quad (1)$$

229 5 km is set as the maximum dilation radius to avoid grouping of too many convective
 230 cores into one object. Core grid points adjoining one another are merged into individual core
 231 objects. Core objects are then horizontally expanded 1 km at a time until they reach another
 232 object or 7 km distance from the core. When they meet another object, they are not merged with
 233 it. This expanded mask around cores encapsulates cells and is applied to track cells more easily
 234 via overlap between the time gap of 15 min. Examples of identified convective cell masks in
 235 observations and the 3-km simulation are shown with black contours in Figure S1. These
 236 convective cells are tracked based on their spatial overlapping masks exceeding 30% between
 237 consecutive timesteps, producing track trajectories like those shown by black lines in Figure S1.
 238 Convective cell advection is estimated using the cross-correlation of reflectivity between
 239 consecutive timesteps and applied to increase the overlapping cell masks between timesteps. The
 240 minimum core area for tracking after dilation is 5 pixels with an area of 45 km^2 . Additional
 241 tracking details are described in Feng et al. (2022). A convective cell is identified as a merger if
 242 it is initially isolated but sufficiently overlaps with another larger cell at the next timestep.
 243 Similarly, a split is a convective cell sufficiently overlapping with a larger cell 1 timestep prior to
 244 being isolated.

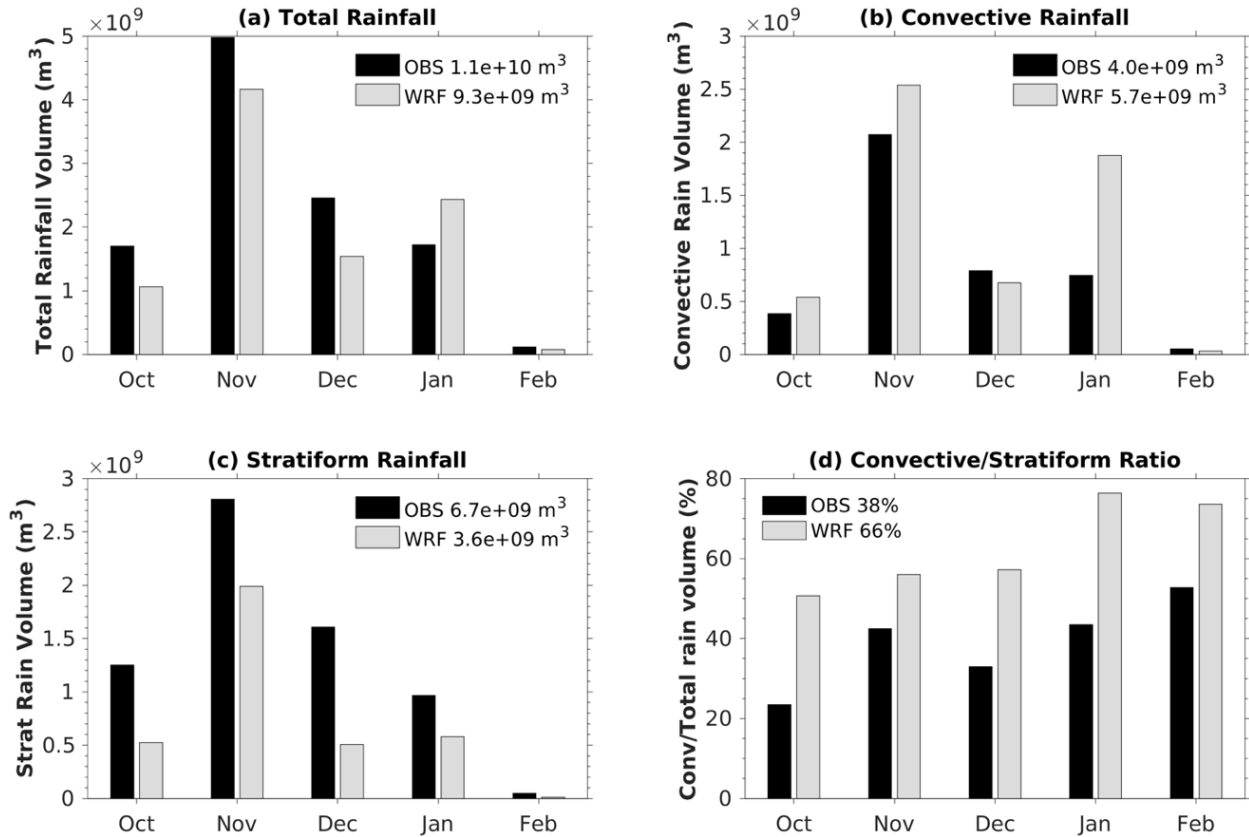
245 In addition to cell tracking for 3-km horizontal grid spacing, a similar algorithm is
246 applied to the CSAPR2 500-m, WRF 1-km, and WRF 0.333-km native grids for obtaining
247 higher-resolution cell tracks. To adapt the tracking to finer grid spacings, the 1-km cell tracking
248 uses a similar core dilation radius as described by Equation 1 but with an adjusted minimum
249 dilation from 3 km to 2 km. The 0.5-km and 0.333-km cell tracking use 1-km minimum core
250 dilation with a minimum core area adjusted from 45 to 13 km². The radius of the region for
251 computing background reflectivity is also reduced from 13.5 km to 11 km in 1-km and 0.333-km
252 settings. In addition, the core expansion into a cell mask is limited to 5 km in these higher
253 resolution runs.

254 All convective cell statistics are computed within their cell masks. Cell areas are defined
255 by the area within the cell masks (black contours in Figure S1) where the composite reflectivity
256 is greater than 10 dBZ. Echo Top Height (ETH) is estimated for each convective cell using the
257 highest altitude where reflectivity exceeds 10 dBZ within the convective cell masks. Convective
258 area and ETH are calculated throughout the lifecycle of convective cell tracks. Cell track
259 initiation times are matched with the INTERPONDE and simulated observing site vertical
260 profile derived environmental conditions at that time. We focus on the most unstable CAPE
261 (MUCAPE, simplified as CAPE hereafter), which is the CAPE associated with the parcel lifted
262 from the level with the maximum equivalent potential temperature in the lower troposphere. The
263 time evolution of CAPE at the CSAPR2 radar location is well reproduced by the season-long
264 simulation, as shown in Zhang et al. (2021). Convective and stratiform rainfall are retrieved from
265 the 2.5-km altitude simulated and CSAPR2 derived rain rates with convective rainfall defined as
266 rain rates within convective cell masks and the rain rates outside convective cell masks defined
267 as stratiform rainfall.

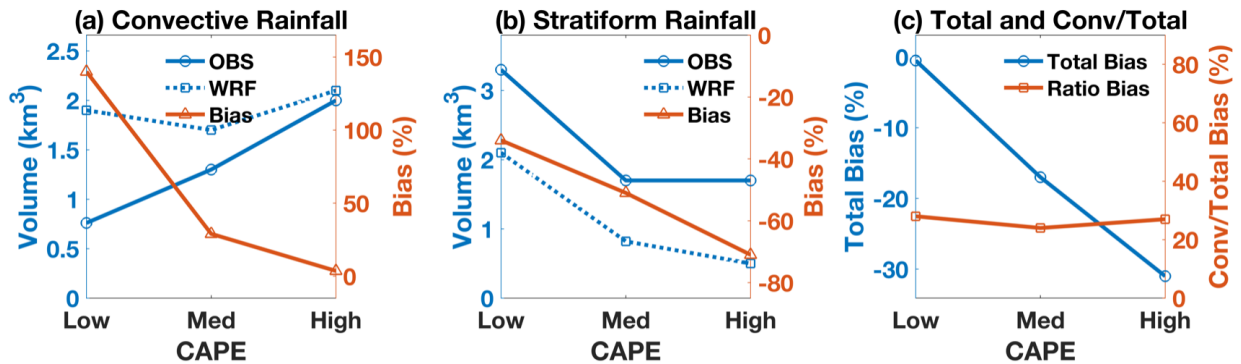
268 **3 Simulated Rainfall Evaluation**

269 The temporal evolution of WRF-simulated rainfall in d3 follows that of observed rainfall
270 estimated from the CSAPR2 radar (Figure S2a), with perhaps a few subtle distinctions. The
271 cumulative rainfall is slightly underestimated by the simulation (Figure S2b) but within the
272 ~15% underestimation that is within the uncertainty expected from blended polarimetric C-band
273 radar rain retrievals in past studies (e.g., Cifelli et al., 2011; Giangrande et al., 2014). The
274 simulation also reproduces the general month-to-month variations in rainfall (Figure 2a).
275 However, dividing the total rainfall into convective and stratiform contributions highlights more
276 significant model biases. The WRF simulation overestimates the convective rainfall by 43%
277 (Figure 2b) while underestimating the stratiform rainfall by 46% (Figure 2c). Thus, the simulated
278 convective to stratiform rainfall volume ratio (66%) is much greater than observed (38%).

279 The simulated convective and stratiform rainfall biases are sensitive to CAPE conditions
280 (Figure 3). The simulated overestimation of convective rainfall decreases as CAPE increases
281 (Figure 3a), while simulated underestimation of stratiform rainfall increases (Figure 3b). Total
282 rainfall is well predicted in low CAPE conditions but becomes increasingly underpredicted as
283 CAPE increases (blue line in Figure 3c). Interestingly, bias in the ratio of convective to total
284 rainfall is not sensitive to CAPE with simulations overestimating the convective contribution by
285 24–28% (orange line in Figure 3c). These values reflect a similar shift to more convective
286 rainfall as CAPE increases in both simulations and observations; however, the simulations have
287 much greater contributions to total rainfall from convective regions for all CAPE conditions.



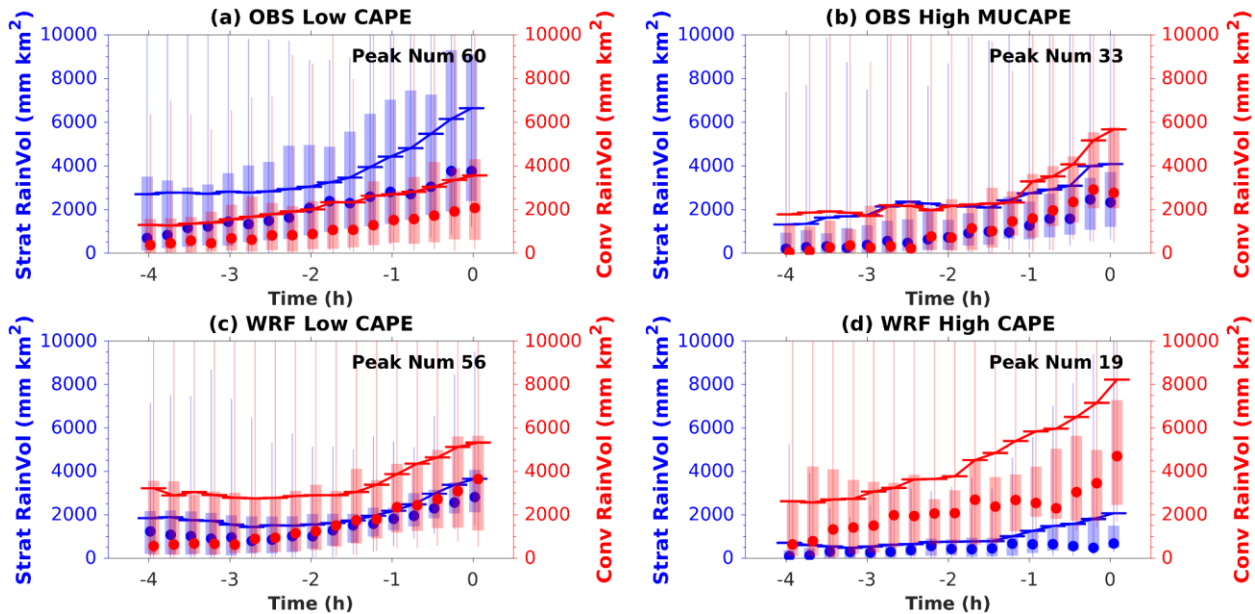
288
289 **Figure 2.** Volume of (a) total, (b) convective, and (c) stratiform rainfall, as well as (d)
290 convective/stratiform rainfall ratio by month with totals over all times shown in the legends.



291
292 **Figure 3.** (a) Convective and (b) stratiform rainfall in observations and simulations with model
293 relative biases as a function of CAPE. (c) Total rainfall relative biases and convective
294 contribution to total rainfall absolute biases conditioned by CAPE.

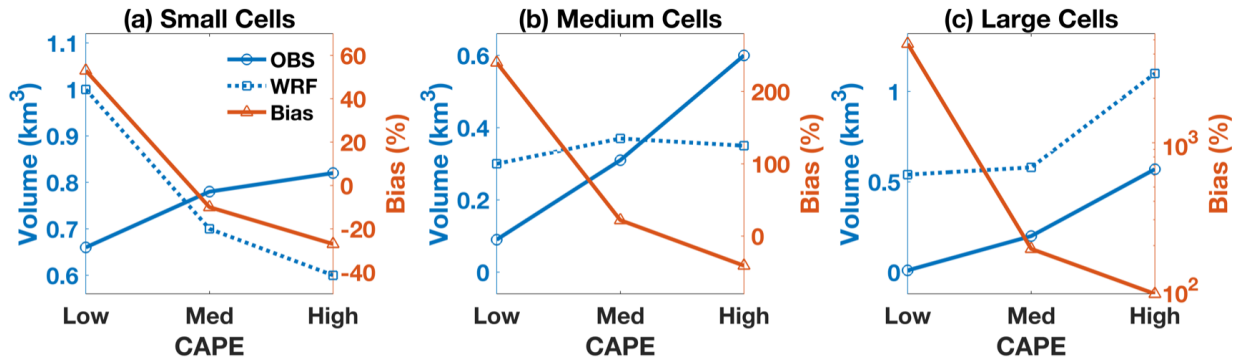
295 Stratiform rainfall volume generally increases with convective rainfall volume (Fig. S3).
296 Their correlation coefficients are between 0.66 and 0.91 depending on CAPE conditions and
297 whether observations or simulations are considered. The correlation coefficients in observations
298 (Figure S3a, c) are lower than those in WRF (Figure S3b, d) because observed stratiform rainfall
299 has a large range when convective rainfall is less than $10,000 \text{ mm km}^2$ with some very large
300 values that are not reproduced in WRF. Even neglecting those values, the observed linear
301 regression slopes are greater than simulated suggesting the model requires more convective
302 rainfall than is observed to yield a similar amount of stratiform rainfall. The regression slopes in

303 higher CAPE conditions are also less than those in lower CAPE conditions by about a factor of
 304 2, meaning high CAPE storms tend to form less stratiform rainfall than low CAPE storms for a
 305 given amount of convective rainfall. This effect is captured by the simulation and might relate to
 306 more intense updrafts in higher CAPE conditions that produce more fast-falling rimed ice, less
 307 snow detrainment, and higher altitude anvils that accentuate sublimation relative to lower CAPE
 308 conditions. All these processes would slow the development of robust stratiform precipitation,
 309 and such processes may be exaggerated in the simulations relative to the observations.



310
 311 **Figure 4.** Stratiform and convective rainfall volume in the 4 hours leading up to the peak rainfall
 312 volume in the domain at time 0 for peak volumes that exceed 2000 mm km². (a–b) Observed and
 313 (c–d) simulated time series are shown for (a, c) low and (b, d) high CAPE conditions. Medians
 314 and means are represented by circles and horizontal lines, respectively. Interquartile and 5th to
 315 95th ranges are shown by the bars and vertical lines, respectively.

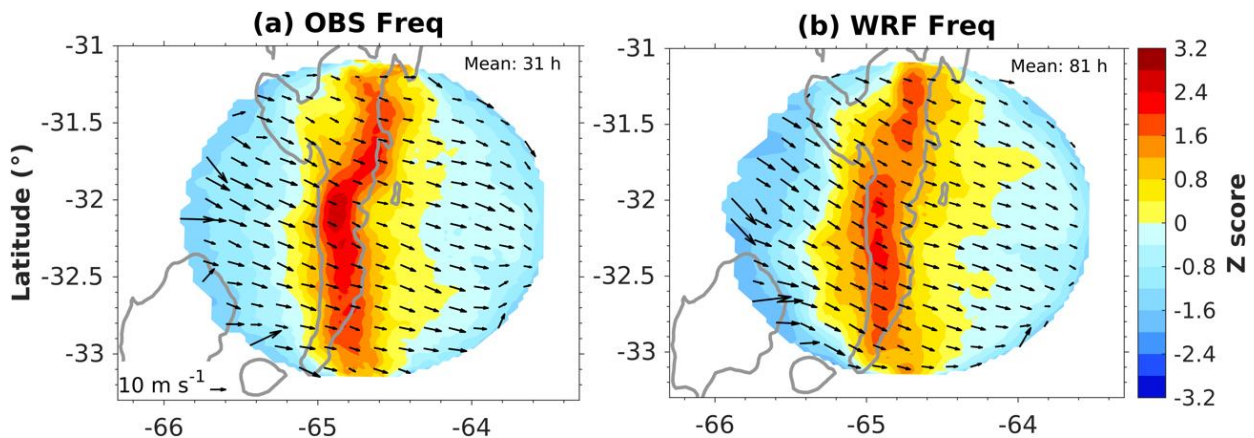
316 The correlation between convective and stratiform rainfall can also be tracked in time to
 317 assess convective and stratiform interactions. The simulation produces a similar number of
 318 rainfall volume peaks > 2000 mm km² to observed in lower CAPE conditions (56 vs. 60; Figure
 319 4a, c) but underestimates the number of peaks in higher CAPE conditions (19 vs. 32; Figure 4b,
 320 d). For lower CAPE, observed stratiform rainfall is always greater than convective rainfall and
 321 grows at a faster rate than convective rainfall within 2 hours of peak total rainfall (Figure 4a). In
 322 contrast, the simulated stratiform rain volume remains lower than the convective rain volume
 323 with a growth rate that is similar or even slightly lesser than the convective growth rate (Figure
 324 4b). Higher CAPE, on the other hand, facilitates more rapid convective growth than stratiform
 325 growth in observations. The simulation reproduces this effect but with much greater convective
 326 precipitation and much lesser stratiform precipitation (Figure 4b, d). This again demonstrates that
 327 the simulation can qualitatively capture the response of convective-stratiform rainfall ratio to
 328 CAPE but is unable to predict its absolute magnitude across CAPE conditions with a bias that is
 329 present throughout the entire growth stage of MCSs.



330
331 **Figure 5.** Cumulative (a) small, (b) medium, and (c) large convective cell rainfall volumes for
332 observations and WRF with relative biases in WRF, conditioned by CAPE.

333 To assess how convective cells contribute to WRF overproduced convective rainfall,
334 Figure 5 shows convective rainfall separated by small ($< 300 \text{ km}^2$), medium ($300\text{--}550 \text{ km}^2$), and
335 large ($> 550 \text{ km}^2$) cells and simulated biases relative to observations. Rainfall produced by small
336 cells is overestimated by the model in low CAPE conditions and underestimated in medium and
337 high CAPE conditions. Medium-sized cell rainfall is overestimated by the model in low and
338 medium CAPE and underestimated in high CAPE. Finally, large cell rainfall is overestimated by
339 the model in all CAPE conditions. For all cell sizes, the observed convective rainfall increases as
340 CAPE increases. However, this is only true for large cells in simulations, and simulated small
341 cell rainfall decreases as CAPE increases. In low CAPE scenarios, all cell sizes contribute to
342 overestimated convective rainfall, whereas in medium and high CAPE scenarios, the larger cells
343 produce overestimated total convective rainfall. Furthermore, model bias increases as cell sizes
344 grow. Clearly, cell properties change differently as a function of CAPE in observations and the
345 simulation. Simulated convective cell biases are further evaluated in Section 4 to reveal potential
346 causes of this difference.

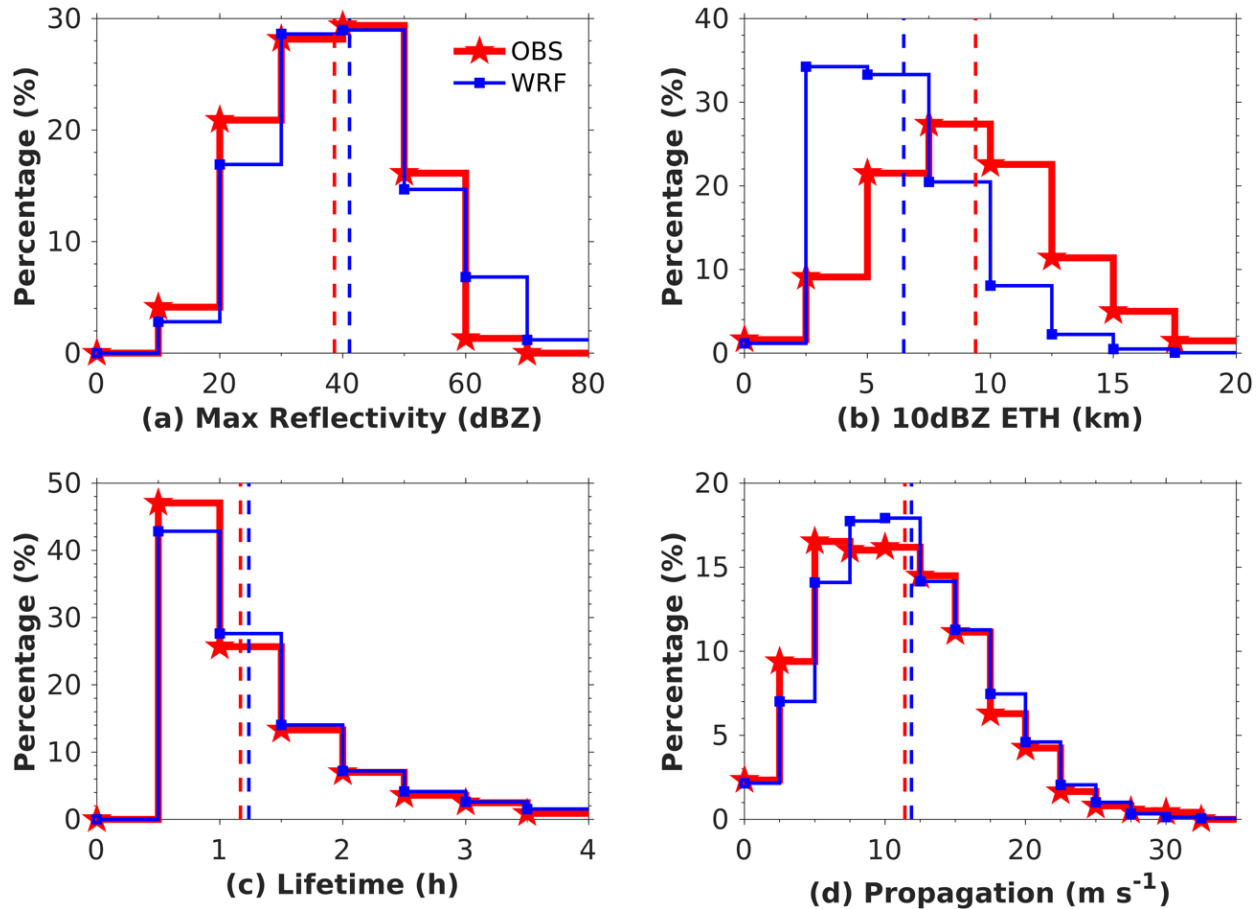
347 **4 Simulated Convective Cell Evaluation**



348
349 **Figure 6.** Spatial occurrence (color fills) and propagation (vector) of (a) observed and (b)
350 simulated convective cell tracks. The Z score is the domain-normalized number of cell hours at a
351 point. Grey contours represent the 1-km terrain height AMSL.

352 There are 5,662 observed and 14,299 simulated convective cells that are tracked; thus, the
353 model produces ~ 2.5 times more cells than are observed. An overestimation of cell number in 3-

354 4 km horizontal grid spacing models with the Thompson scheme including HRRR has been
 355 noted previously (Clark et al., 2014; Duda and Turner, 2021, 2023), though such a large bias is
 356 not seen for the number of convective systems using reflectivity-based objects (e.g., Grim et al.,
 357 2021). 2,355 observed and 6,016 simulated convective cells initiate and grow (by reflectivity
 358 area) within the domain, and these are used in further analyses. The simulation reproduces the
 359 spatial distribution of these cells, with the highest frequency centered over the SDC range just
 360 east of the highest ridgeline (Figure 6). The eastward propagation of these cells is also captured
 361 by the simulation, suggesting that it reasonably captures the processes controlling the
 362 spatiotemporal distribution of moist convection despite more numerous cells that may thus be the
 363 result of convective scale processes.



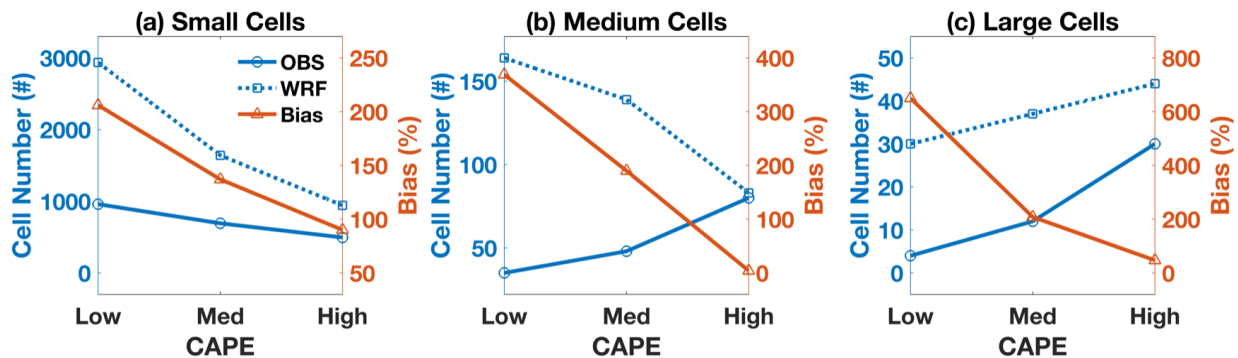
364 **Figure 7.** Probability distributions of convective cell (a) lifecycle-maximum reflectivity, (b)
 365 10-dBZ ETH, (c) lifetime, and (d) propagation speed. Red and blue dashed vertical lines represent
 366 the mean values in observations and simulations, respectively.
 367

368 The simulation also generally captures the peak probabilities of convective cell maximum
 369 reflectivity, lifetime, and propagation speed (Figure 7a, c, and d), though with a slight bias
 370 toward greater values. The greater occurrence of simulated reflectivities exceeding 60 dBZ could
 371 be related to the observed reflectivities being C-band in which large hydrometeors such as hail
 372 can produce non-Rayleigh scattering, whereas WRF reflectivities are estimated assuming purely
 373 Rayleigh scattering. The reflectivity difference is unsurprising based on previous studies (e.g.,
 374 Varble et al. 2011). Differences between observation and simulation mean values are more
 375 substantial for ETH (Figure 7b). The model greatly overestimates the probability of shallow

376 convective cells (ETH = 2.5–7.5 km) and underestimates the probability of deep convection
 377 (maximum ETH > 7.5 km). Part of this difference is due to non-uniform beam filling and
 378 extrapolation artifacts in the Cartesian gridding of observations that results in an ETH high bias.

379 The high bias in simulated cell number is most apparent in low CAPE conditions for all
 380 cell areas and decreases as CAPE increases (Figure 8). However, the model produces more
 381 numerous convective cells across all CAPE conditions for all convective cell areas. The cell
 382 number bias also increases with the cell area in low CAPE conditions. However, in high CAPE
 383 conditions, the WRF overestimation of cell number decreases from small to medium area cells
 384 and increases from medium to large cells. This indicates potentially different process controls on
 385 cell size distributions in high CAPE relative to low CAPE conditions.

386 In addition to convective cell number, the convective cell area differences between the
 387 simulation and observations vary by CAPE. Simulated convective cell areas are larger than
 388 observed in low-medium CAPE conditions but the probability of large convective cells in high
 389 CAPE conditions is underestimated (Figure S4). Recall that the model overestimation of total
 390 convective rainfall decreases with CAPE, partially a result of the model overestimation of
 391 convective cell number decreasing with CAPE (particularly for large cells that produce the
 392 heaviest rainfall). The change in convective rainfall volume biases as cell area changes also far
 393 exceeds the change in convective cell number biases (Figure 5 vs. Figure 8).

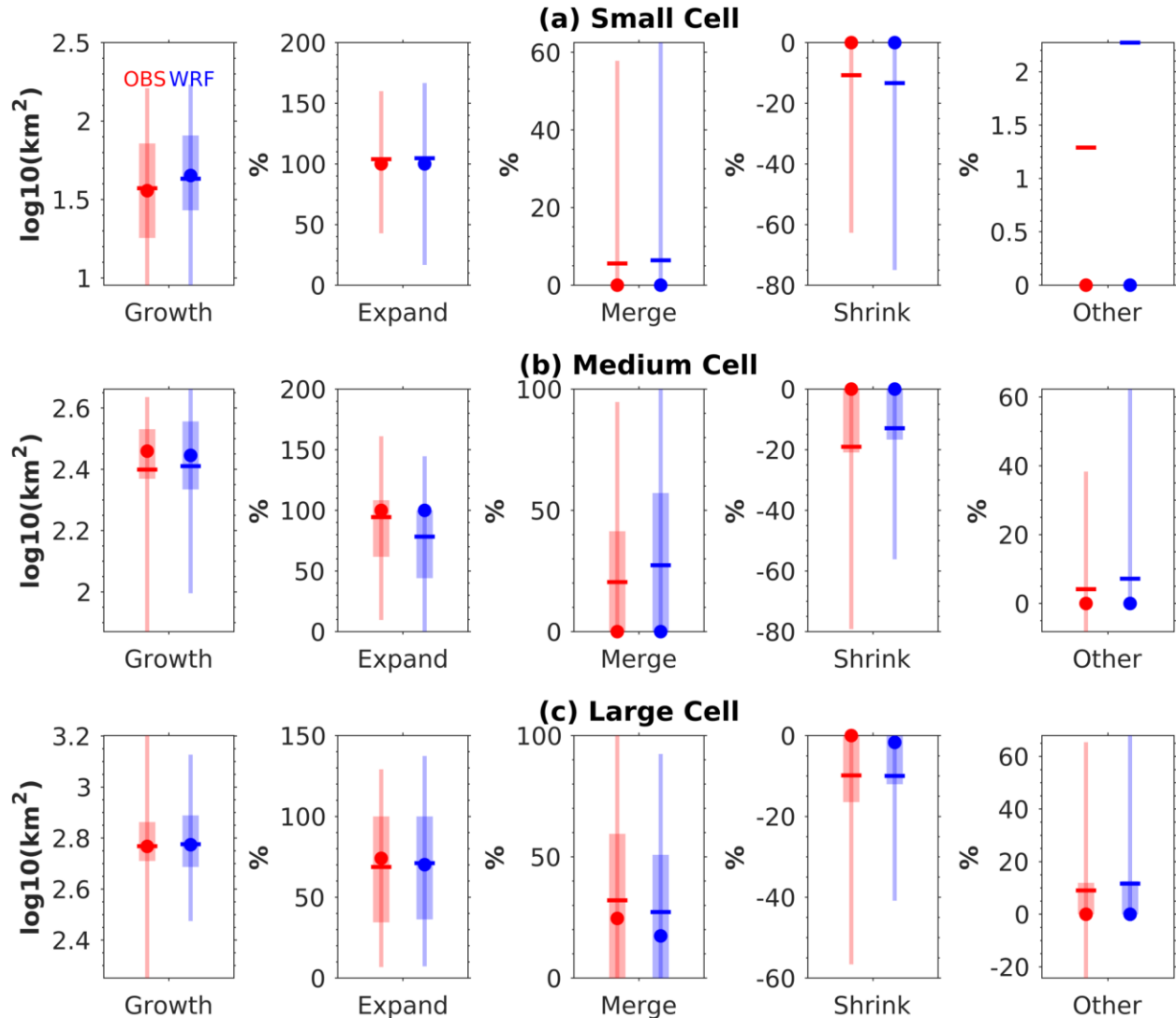


394
 395 **Figure 8.** Observed and simulated (a) small, (b) medium, and (c) large convective cell track
 396 numbers and WRF biases relative to observed, conditioned by CAPE.

397 Given the differences in observed and simulated cell properties, convective cell net
 398 growth is explored for the lifecycle growth period between the cell initiation and the lifecycle
 399 maximum cell area times. Net growth during this lifecycle period is controlled by convective cell
 400 expanding, shrinking, merging, and splitting processes, which are quantified and evaluated in
 401 Figure 9. Merging and splitting areas are the cell area difference between the two consecutive
 402 timesteps over which merging or splitting occurs and includes the potential shrinking and
 403 expansion during that period. Since a pure split is uncommon in both the observations and
 404 simulation, splits are combined with splits plus mergers occurring at the same time into the
 405 “other” category.

406 The mean and interquartile range values of the simulated small cell net growth are greater
 407 than observed. Observed and simulated cell expansion contributions to cell growth are both near
 408 100% on average, with fewer contributions from shrinking, merging, and splitting. This indicates
 409 that small cell expansion growth dominates the observation-simulation net growth difference.
 410 However, medium area cell growth (Figure 9b) is underestimated by the model. Simulated

411 medium area cell shrinking is slightly underestimated and the simulated merging is slightly
 412 greater than observed, but these are not able to counteract the dominant control of cell expansion,
 413 which is greater in observations. The mean and median simulated large cell net growth and
 414 expansion are similar to observed (Figure 9c), which is the result of combined overestimated
 415 expansion and underestimated merging in the simulation. Thus, despite differences in observed
 416 and simulated cell numbers, areas, and contributions to rainfall, there are limited differences in
 417 cell area growth lifecycles.

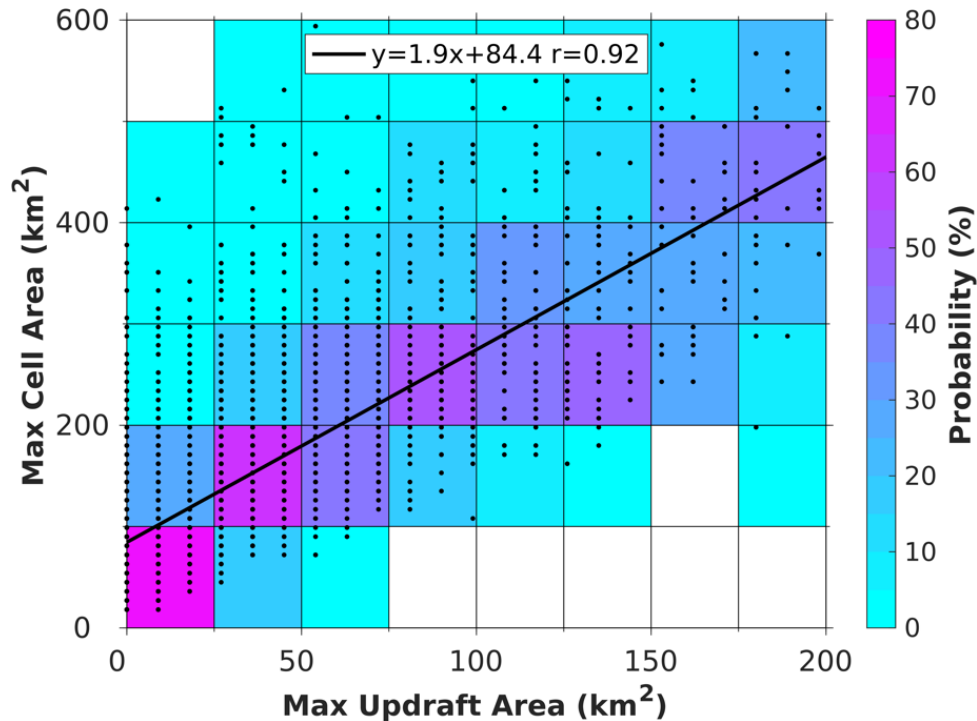


418 **Figure 9.** Observed (red) and simulated (blue) convective cell area net growth with contributions
 419 from cell expansion, merging, shrinking, and other (splitting, splitting plus merging) during the
 420 growth period between initiation and lifetime-maximum area across all CAPE conditions. Means
 421 and medians are represented by circles and horizontal lines, respectively. Interquartile and 5th to
 422 95th ranges are shown by bars and vertical lines, respectively.

424 **5 Physical Controls on Convective Cell Biases**

425 Convective updraft area is calculated throughout each individual convective cell lifecycle
 426 in the simulation. Updraft regions are defined as having vertical velocity greater than 2 m s^{-1} and

427 radar reflectivity greater than 10 dBZ within the identified convective cell footprints. Figure 10
 428 shows that the lifecycle- and column-maximum convective updraft area positively correlates
 429 with the lifecycle-maximum aggregated convective cell area with a linear correlation coefficient
 430 higher than 0.9 ($r = 0.85\text{--}0.96$ for 200,000 times of random bootstrapping), indicating a robust
 431 positive correlation. The maximum convective cell area reached is usually twice the column-
 432 maximum updraft area reached during a cell's lifecycle, though this ratio is sensitive to the
 433 definition of the updraft and cell area.



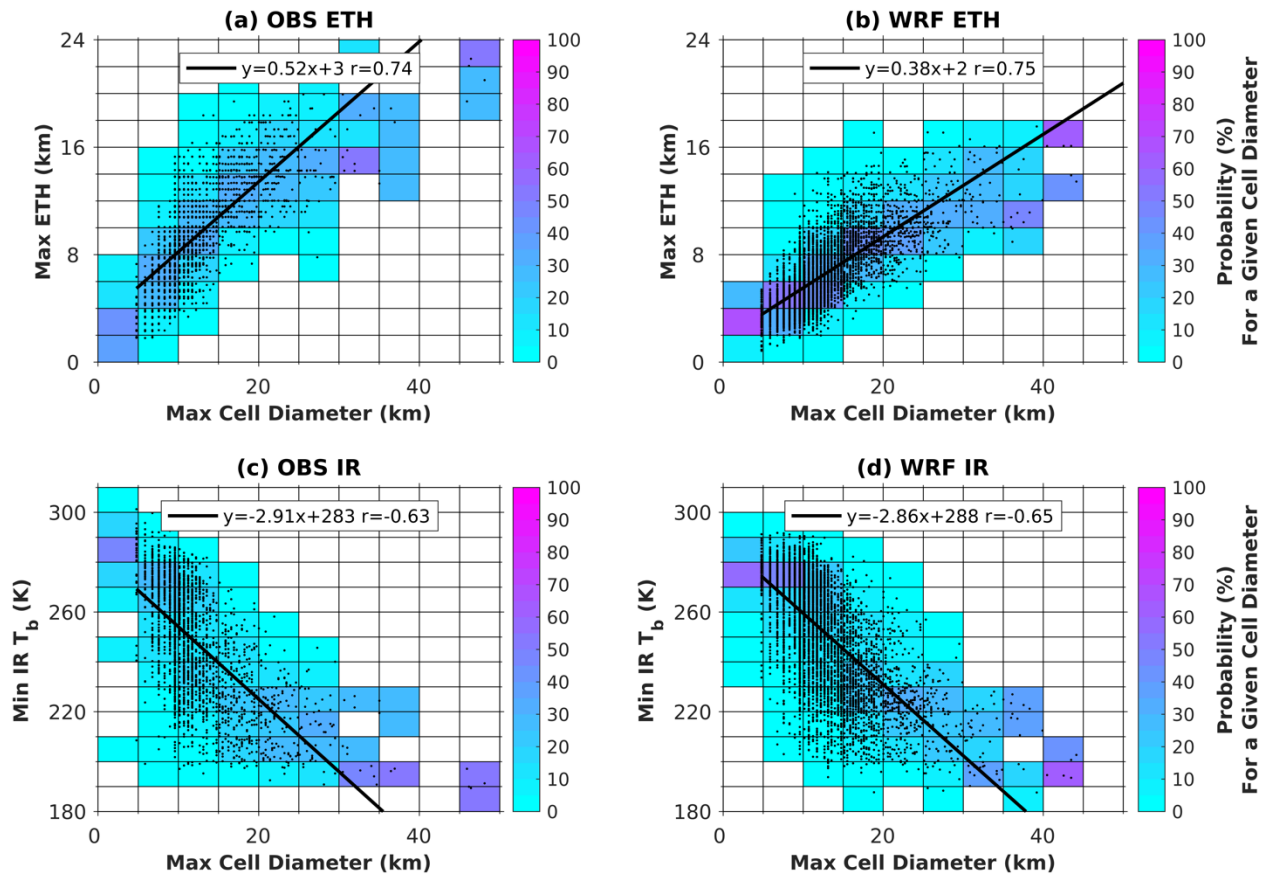
434
 435 **Figure 10.** Lifecycle-maximum convective cell area as a function of lifecycle- and column-
 436 maximum updraft area. The color fill shows cell area probabilities conditioned on maximum
 437 updraft area, i.e., within each maximum updraft area bin.

438 Relationships of the lifecycle-maximum convective cell circle-equivalent diameter
 439 ($2\sqrt{\text{Area}/\pi}$) with the lifecycle-maximum 10-dBZ radar reflectivity ETH and lifecycle-minimum
 440 TOA IR T_b can inform potential observed and simulated updraft differences. In Figure 11, the
 441 highest observed ETHs reach 22 km, which is higher than those simulated, which reach 18 km,
 442 consistent with Figure 7b. The simulated linear regression slope between cell diameter and ETH
 443 (0.38) is lower than observed (0.52), indicating cells reach greater depths for a given cell area in
 444 observations as compared to the simulation.

445 Due to Cartesian gridding artifacts, non-uniform radar beam filling, and sidelobe
 446 contamination, the ETH estimated from ground-based radar measurements tends to be biased
 447 high (e.g., Lakshmanan et al., 2013), which likely contributes to the model-observation ETH
 448 difference. The TOA IR T_b measured by GOES-16 is re-gridded to WRF 3-km grids for
 449 comparison with simulated TOA IR T_b empirically derived from the simulated outgoing
 450 longwave radiation, following the approach in (Yang & Slingo, 2001). Higher TOA IR T_b
 451 indicates that the cloud top has more outgoing longwave radiation, which corresponds to a lower,
 452 warmer cloud top. The simulated lifecycle-minimum TOA IR T_b range of values agrees with that

453 observed, but the absolute value of the regression slope in the simulation is slightly less steep
 454 than observed (Figure 11c–d). That means for a given cell diameter, the simulation is more likely
 455 to have a lower cloud top than observed. This agrees with the radar ETH bias as a function of cell
 456 diameter, but with a much smaller difference, suggesting that a significant portion but not all the
 457 radar ETH difference is a retrieval artifact.

458 These relationships of convective updraft and cell properties suggest that convective cell
 459 area is a good qualitative proxy for updraft area and depth in the simulation. Although updraft
 460 properties are not directly retrievable from observations, it is physically plausible that observed
 461 cell area and depth also scale with updraft area (though potentially with a different slope). It is
 462 also plausible that the widest, deepest updrafts exist in relatively high CAPE conditions. This
 463 suggests that updraft widths would be least resolved in simulated low CAPE conditions, which is
 464 indeed where the largest model biases are found.



465 **Figure 11.** Observed and simulated (a–b) lifecycle-maximum 10-dBZ radar reflectivity ETH and
 466 (c–d) lifecycle-minimum TOA IR T_b as functions of lifecycle-maximum convective cell
 467 diameter. The color fill shows ETH and TOA IR T_b probabilities conditioned on maximum cell
 468 diameter. The ordinary least square fit lines are shown in black, and the r value represents the
 469 Pearson linear correlation coefficient.
 470

471 Excessive numbers of shallow cells in the simulation bring the average cell depth down
 472 for a given cell width, which may negatively impact stratiform rainfall formation. Convective
 473 cells that do not reach well above the freezing level likely have limited ice detrainment that is
 474 critical to the formation of stratiform anvil regions, and the simulation has excessive numbers of
 475 these cells. It is also possible that the deep cells in the simulation fail to detrain vapor-grown ice

476 in sufficient amounts over sufficient height layers to adequately grow precipitating stratiform
477 regions as highlighted in previous studies (Varble et al. 2014b, Han et al. 2019). In this scenario,
478 underproduced stratiform precipitation in the simulation results in less extensive atmospheric
479 stabilization caused by its upper-level latent heating over lower-level latent cooling. Such a
480 process would leave more atmospheric instability to be consumed by additional convective cells.
481 Thus, there could exist a positive feedback between the convective cell and stratiform biases, and
482 such interactions deserve further investigation in the future.

483 Additional possible causes for excessive numbers of shallow convective cells are biased
484 dynamical and/or microphysical processes. Focusing on possible dynamical biases, convective
485 updrafts are severely under-resolved for 3-km horizontal model grid spacing, resulting in wider
486 simulated updrafts than those in the real world. For relatively shallow cells with small areal
487 coverage, updrafts are thinnest and thus potentially the most biased too wide, which could
488 suppress entrainment dilution but enhance opposing vertical pressure gradients. The minimum
489 resolved wavelength by WRF is approximately 7 times the grid spacing (Skamarock, 2004).
490 Thus, despite explicit convection, this simulation at 3-km grid spacing only fully resolves a half
491 wavelength feature like a convective updraft if it is 10.5 km or more wide, corresponding to a
492 circular convective updraft area of 87 km² and a cell area that is typically twice the updraft area
493 (174 km²). This is substantially wider than most convective updrafts measured by aircraft (e.g.,
494 (Warner & McNamara, 1984; Lucas et al., 1994; Anderson et al., 2005) and radar wind profilers
495 (e.g., Wang et al., 2020). Indeed, more than 2/3 of convective cell areas defined on a 500-m
496 spaced grid are smaller than the minimum resolvable areal threshold (174 km²) at 3-km grid
497 spacing (Figure S5). This could result in a shift of energy from unresolvable small cells into
498 larger resolvable cell sizes in the simulation, possibly contributing to the previously discussed
499 model biases.

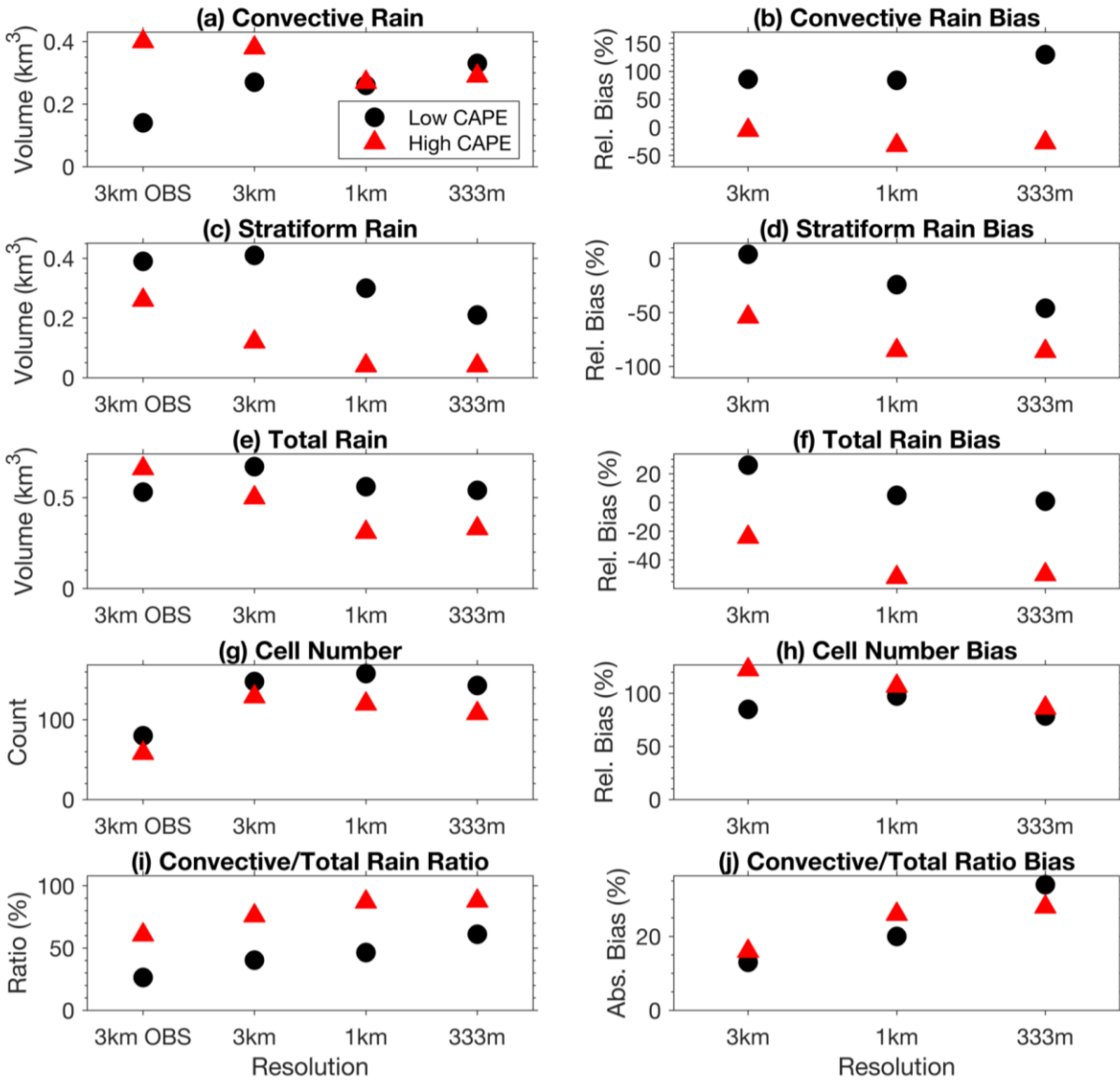
500 **6 Bias Sensitivity to Model Resolution**

501 To test how increased model resolution affects simulated convective cell and convective-
502 stratiform partitioning biases, low and high CAPE events were chosen (Table 1) and simulated
503 with nested 1- and 0.333-km horizontal grid spacing domains to compare with the 3-km grid
504 spacing results (see Section 2.2 for details). Observations were also analyzed on a 500-m
505 horizontal grid in addition to the 3-km grid. All results in this section apply to the individual low
506 and high CAPE events, though 3-km results are generally consistent with the season-long
507 simulation results.

508 In the low CAPE case (black dots in Figure 12), convective rain volumes are
509 overestimated by more than 84% in all 3 simulations (Figure 12b). The simulated convective rain
510 volumes in the 3-km and 1-km runs are similar, but the 0.333-km run produces about 25% more
511 convective rainfall than coarser simulations (Figure 12a). Figure 12c–d shows that the 3-km run
512 accurately predicts the stratiform rainfall, but the 1-km and 0.333-km runs underestimate it by 24
513 and 46%, respectively. In Figure 12e–f, 1-km and 0.333-km convective and stratiform biases
514 offset to produce total rainfall that is similar to observed in the low CAPE case while the 3-km
515 run overestimates rainfall by 26%. In Figure 12g–h, simulated cell numbers are nearly double
516 those observed for all resolutions with the 1-km experiment producing the most numerous
517 convective cells.

518 In contrast to the low CAPE case, the high CAPE case's convective rainfall is simulated
519 accurately in the 3-km run but underestimated by ~30% in the 1-km and 0.333-km simulations

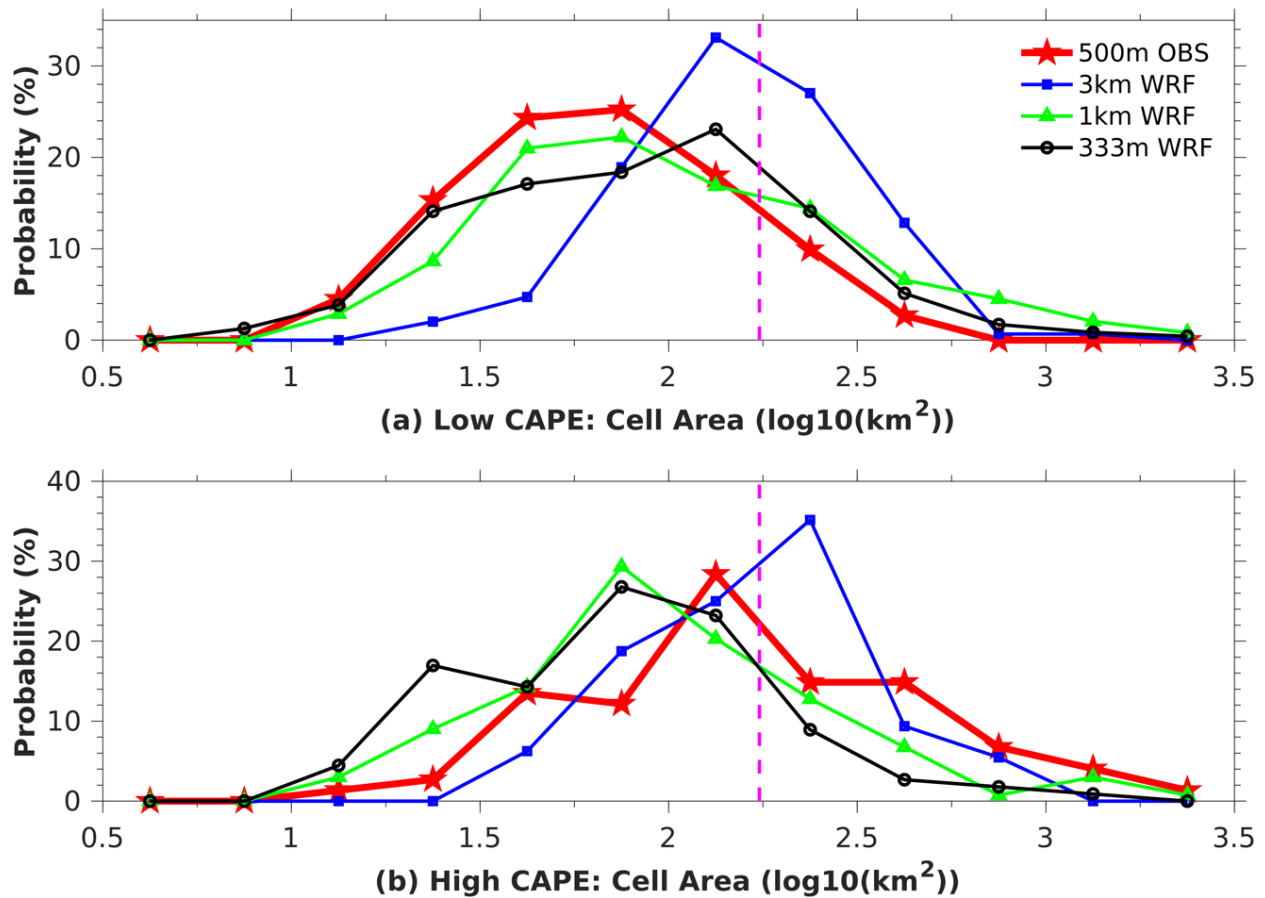
520 (Figure 12a-b). Stratiform rainfall is greatly underestimated by the simulations, a bias that
 521 increases from -54% to -86% as horizontal grid spacing decreases from 3 to 0.333 km and is
 522 much worse than the low CAPE stratiform rainfall bias. The stratiform underproduction leads to
 523 total rainfall being underestimated by all simulations with 1-km and 0.333-km runs producing
 524 only half of what was observed due to additional contributions from underpredicted convective
 525 rainfall (Figure 12c-d). Simulated convective cell numbers are about double those observed for
 526 all model resolutions, similar to the low CAPE case (Figure 12g-h).



527 **Figure 12.** Rainfall and cell number statistics for 3-, 1-, and 0.333-km horizontal grid spacing
 528 simulations and 3-km horizontal grid spacing observations with biases relative to observations
 529 for the low and high CAPE events.
 530

531 The convective contribution to total rainfall (Figure 12i-j) is also biased high for all
 532 simulations and increases as resolution increases for both low and high CAPE cases. Overall,
 533 stratiform rainfall biases and their biased contribution to total rainfall worsen as the model grid
 534 spacing decreases in these convective cases. This suggests that effectively reducing the

535 stratiform bias cannot be achieved solely via increasing the model’s resolution, pointing to
 536 physics parameterization contributions that require further evaluation. Additionally, some biases
 537 do not monotonically change with model resolution and vary between low and high CAPE cases,
 538 which agrees with some past studies (e.g., Bryan et al., 2003; Prein et al., 2021).



539 **Figure 13.** Probability distributions of convective cell areas for the (a) low and (b) high CAPE
 540 events for full resolution datasets (not averaged to 3-km grid spacing) except for the 0.333-km
 541 run that is averaged to 500 m to match 500-m observations. The vertical dashed lines represent
 542 the approximate minimum resolvable cell area in WRF with 3-km horizontal grid spacing.
 543

544 Convective cell properties also vary substantially by resolution. In the low CAPE event,
 545 the 3-km run significantly underestimates the probability of convective cells at sizes smaller than
 546 80 km² (Figure 13a; 1.9 on the log10 scale). The 1-km run produces many more cells that are
 547 smaller than the 3-km run’s effective resolution, but still with cell areas shifted slightly larger
 548 than observed. The 0.333-km run agrees best with the observed distribution, indicating that
 549 decreasing model grid spacing below 500 m may be required to adequately resolve the cell area
 550 distribution in some conditions. Kolmogorov-Smirnov (KS) testing of differences between
 551 observed and simulated cell area distributions further demonstrates that p values increase as
 552 model resolution increases from 5×10^{-13} to 0.007 and 0.05 for 3-, 1-, and 0.333-km runs,
 553 respectively. Thus, at a 5% level, 3-km and 1-km runs significantly differ from observations
 554 while the simulated area distribution in the 0.333-km run does not. In the high CAPE event, the
 555 observed convective cells are larger than those in the low CAPE case (Figure 13). More
 556 convective cells in the 3-km simulation are shifted to the right side of the dashed line and better

557 resolved in these conditions as compared to the low CAPE event. The 3-km run also better
558 agrees with the observed cell area distribution for this high CAPE event (p value = 0.1) than the
559 1-km and 0.333-km runs (p values of 0.001 and 0.0001, respectively). The simulated updraft
560 width distribution differences (Figure S6) largely follow the cell area distribution differences in
561 Figure 13, showing that updrafts become better resolved with increasing resolution with cell
562 areas being a decent proxy for updraft area. However, all resolutions fail to reproduce the notable
563 shift from small to large cell sizes that is observed with increasing CAPE (Figure 13a–b) without
564 universal improvement of cell areas with resolution across both low and high CAPE conditions.

565 Despite shifts to smaller cell and updraft areas as model resolution increases, Figure S7
566 shows that convective cell depth is greatly underestimated across all resolutions in both low and
567 high CAPE conditions. Thus, all simulations, regardless of resolution, produce more numerous
568 shallow cells than observed that dominate the PDFs, with the caveat that a portion of the
569 difference is also due to high biased ETHs in observations. In both low and high CAPE events,
570 simulated shallow cell echo tops peak between 4 and 7 km AMSL. The excessive number of
571 these relatively shallow cells amplify convective rainfall with little contribution to stratiform
572 rainfall growth. Collectively, the model resolution sensitivity tests suggest that insufficient
573 model resolution is not the primary cause for convective cell area, depth, and stratiform growth
574 biases. This suggests that physics parameterizations such as the microphysics scheme's control
575 on precipitation formation and growth are potentially primary contributors to cell number, cell
576 depth, and convective-stratiform partitioning biases.

577 **7 Conclusions**

578 This study evaluated the accuracy of convective cell and system growth in a season-long
579 convection-permitting WRF simulation with 3-km horizontal grid spacing using RELAMPAGO-
580 CACTI field campaign measurements. Observed and simulated cells were analogously defined
581 and tracked with results assessed in the context of atmospheric instability as represented by
582 CAPE, which was found to modulate model biases.

583 The simulation reproduced the observed total rainfall in low CAPE conditions and only
584 slightly underestimated it in high CAPE conditions. However, when separating rainfall into
585 convective and stratiform components, large biases were found, including:

- 586 • Convective rainfall was overestimated by 43% in the simulation, a bias that decreased
587 with CAPE. However, simulated stratiform rainfall was underestimated by 46%, a bias
588 that increased with CAPE.
- 589 • Stratiform rainfall increased with convective rainfall, but the simulation required about
590 double the convective rainfall to produce a similar amount of stratiform rainfall as that
591 observed.
- 592 • The large model overestimation of the convective contribution to total rainfall remained
593 approximately constant at 26% through all CAPE conditions.

594 Convective and stratiform rainfall partitioning biases were related to the model
595 representation of convective cell number, area, depth, and growth characteristics, producing the
596 following results:

- 597 • The simulation contained 2.6 times the number of cells that were observed, primarily
598 through the production of excessive numbers of relatively shallow cells (4-7-km cell

599 tops). The model required a wider convective cell to reach the same convective depth as
600 observed.

- 601 • The overproduction of simulated cells increases as CAPE decreases, potentially because
602 these conditions are anticipated to result in more numerous shallow and narrow updrafts
603 as compared to high CAPE conditions. The cell number overestimation also increases as
604 cell area increased in low CAPE conditions, but the overestimation does not
605 systematically change with cell area in high CAPE conditions.
- 606 • Relatively large cells contributed the most to convective rainfall biases, with
607 contributions increasing as CAPE decreased. Despite this, cell growth processes via
608 expansion, shrinking, merging, and splitting show limited differences between
609 observations and the simulation.

610 Finally, possible controls of model resolution upon simulated convective cell biases were
611 investigated in simulations of representative cases containing low and high CAPE conditions
612 using 3-km, 1-km, and 0.333-km horizontal grid spacing. Simulated convective cell area was
613 proportional to updraft area, indicating that radar reflectivity observations may be able to inform
614 updraft width. A large proportion of convective cell areas defined using 500-m grid spacing
615 radar observations were not fully resolvable with 3-km horizontal grid spacing in WRF, with
616 small area cells that reached depths of less than 7 km being the worst resolved. Comparing
617 analogous cell precipitation characteristics across model resolutions resulted in the following
618 conclusions:

- 619 • The high cell number bias noted in the 3-km simulation was not mitigated by increasing
620 model grid resolution.
- 621 • Despite better spatially resolving convective updrafts and cells, increasing model
622 resolution amplified the simulated underestimation of stratiform rainfall and the
623 overestimation of convective contribution to total rainfall.
- 624 • Total rainfall and cell areas during the low CAPE event were best captured by the 0.333-
625 km run. However, these properties were best captured by the 3-km run during the high
626 CAPE event.

627 This study implies that substantial convective cell and system rainfall biases can exist in
628 continental convection-permitting simulations with settings commonly used in regional weather
629 and climate modeling with strong modulation by environmental instability. Increasing model
630 resolution by an order of magnitude neither reduces excessive numbers of precipitating
631 congestus clouds nor decreases ratios of convective to stratiform precipitation, suggesting that
632 improving prediction of deep convective system growth depends on factors beyond solely
633 increasing model resolution. Following findings in past studies, a potentially substantial
634 contributor to biases is the cloud microphysics parameterization that may promote too efficient
635 precipitation formation and growth in congestus clouds with excessive supercooled liquid and
636 riming in mixed phase clouds, which would strongly modulate convective cell identification and
637 convective-stratiform precipitation partitioning. Further work is required to assess how well
638 these findings correspond to other model setups with different environmental conditions. In
639 addition, research is required to assess the speculated physical pathways by which convective
640 cell and stratiform rainfall biases emerge such that they can be mitigated.

641 **Acknowledgments**

642 The study was funded by NSF project 1661662 and the U.S. Department of Energy
 643 (DOE) Office of Science Biological and Environmental Research as part of the Atmospheric
 644 System Research program. Pacific Northwest National Laboratory is operated by Battelle for the
 645 U.S. Department of Energy under Contract DE-AC05-76RLO1830. Computing and disk storage
 646 resources were provided by the NCAR Computational and Information Systems Laboratory and
 647 the University of Utah Center for High Performance Computing. Some data analysis was also
 648 performed using computational resources provided by the National Energy Research Scientific
 649 Computing Center, a DOE Office of Science User Facility supported under contract DE-AC02-
 650 05CH11231. We thank K. Ryder Fox (University of Miami) for contributing to the LES setup.

651 **Open Research**

652 The model setup for WRF runs and the observed and simulated convective cell track
 653 datasets are available here: <https://doi.org/10.5281/zenodo.10655168> (Zhang et al., 2024). The
 654 PyFLEXTRKR software, designed for convective cell tracking, is openly available for download
 655 at GitHub repository: <https://github.com/FlexTRKR/PyFLEXTRKR>. The configuration for
 656 PyFLEXTRKR in this study can be accessed via at GitHub repository:
 657 https://github.com/zhixiaozhang/cacti_cell_tracking_config. The radar measurements, satellite
 658 retrievals, and raw model output are large datasets that can be accessed by contacting the
 659 authors.

660 **References**

- 661 Anderson, N. F., Grainger, C. A., & Stith, J. L. (2005). Characteristics of strong updrafts in
 662 precipitation systems over the central Tropical Pacific Ocean and in the Amazon. *Journal of*
 663 *Applied Meteorology*, *44*(5), 731-738. <https://doi.org/10.1175/JAM2231.1>
- 664 Bretherton, C. S., & Park, S. (2009). A new moist turbulence parameterization in the Community
 665 Atmosphere Model. *Journal of Climate*, *22*(12), 3422-3448.
 666 <https://doi.org/10.1175/2008JCLI2556.1>
- 667 Bringi, V. N., & Chandrasekar, V. (2001). *Polarimetric Doppler Weather Radar: Principles and*
 668 *Applications*. Cambridge University Press. <https://doi.org/10.1017/CBO9780511541094>
- 669 Bryan, G. H., Wyngaard, J. C., & Fritsch, J. M. (2003). Resolution requirements for the
 670 simulation of deep moist convection. *Monthly Weather Review*, *131*(10), 2394-2416.
 671 [https://doi.org/10.1175/1520-0493\(2003\)131<2394:RRFTSO>2.0.CO;2](https://doi.org/10.1175/1520-0493(2003)131<2394:RRFTSO>2.0.CO;2)
- 672 Bryan, G. H., & Morrison, H. (2012). Sensitivity of a simulated squall line to horizontal
 673 resolution and parameterization of microphysics. *Monthly Weather Review*, *140*(1), 202–
 674 225. <https://doi.org/10.1175/MWR-D-11-00046.1>
- 675 Caine, S., Lane, T. P., May, P. T., Jakob, C., Siems, S. T., Manton, M. J., & Pinto, J. (2013).
 676 Statistical assessment of tropical convection-permitting model simulations using a cell-
 677 tracking algorithm. *Monthly Weather Review*, *141*(2), 557-581.
 678 <https://doi.org/10.1175/MWR-D-11-00274.1>
- 679 Casaretto, G., Dillon, M. E., Salio, P., Skaba, Y. G., Nesbitt, S. W., Schumacher, R. S., et al.
 680 (2021). High-resolution NWP forecast precipitation comparison over complex terrain of the
 681 Sierras de Córdoba during RELAMPAGO-CACTI. *Weather and Forecasting*, *37*(2), 241-
 682 266. <https://doi.org/10.1175/WAF-D-21-0006.1>

- 683 Chen, S. S., & Frank, W. M. (1993). A numerical study of the genesis of extratropical convective
684 mesovortices. Part I: evolution and dynamics. *Journal of the Atmospheric Sciences*, 50(15),
685 2401-2426 [https://doi.org/10.1175/1520-0469\(1993\)050<2401:ANSOTG>2.0.CO;2](https://doi.org/10.1175/1520-0469(1993)050<2401:ANSOTG>2.0.CO;2)
- 686 Cifelli, R., Chandrasekar, V., Lim, S., Kennedy, P. C., Wang, Y., & Rutledge, S. A. (2011). A
687 new dual-polarization radar rainfall algorithm: Application in Colorado precipitation events.
688 *Journal of Atmospheric and Oceanic Technology*, 28(3), 352-364.
689 <https://doi.org/10.1175/2010JTECHA1488.1>
- 690 Clark, A. J., Bullock, R. G., Jensen, T. L., Xue, M., & Kong, F. (2014). Application of object-
691 based time-domain diagnostics for tracking precipitation systems in convection-allowing
692 models. *Weather and Forecasting*, 29(3), 517-542. <https://doi.org/10.1175/WAF-D-13-0098.1>
- 694 Craig, G. C., & Dörnbrack, A. (2008). Entrainment in cumulus clouds: What resolution is cloud-
695 resolving? *Journal of the Atmospheric Sciences*, 65(12), 3978-3988.
696 <https://doi.org/10.1175/2008JAS2613.1>
- 697 Donner, L. J. (1993). A cumulus parameterization including mass fluxes, vertical momentum
698 dynamics, and mesoscale effects. *Journal of the Atmospheric Sciences*, 50(6), 889-906.
699 [https://doi.org/10.1175/1520-0469\(1993\)050<0889:ACPIMF>2.0.CO;2](https://doi.org/10.1175/1520-0469(1993)050<0889:ACPIMF>2.0.CO;2)
- 700 Donner, Leo J., Seman, C. J., Hemler, R. S., & Fan, S. (2001). A cumulus parameterization
701 including mass fluxes, convective vertical velocities, and mesoscale effects:
702 Thermodynamic and hydrological aspects in a general circulation model. *Journal of*
703 *Climate*, 14(16), 3444-3463. [https://doi.org/10.1175/1520-0442\(2001\)014<3444:ACPIMF>2.0.CO;2](https://doi.org/10.1175/1520-0442(2001)014<3444:ACPIMF>2.0.CO;2)
- 705 Dowell, D. C., Alexander, C. R., James, E. P., Weygandt, S. S., Benjamin, S. G., Manikin, G. S.,
706 et al. (2022). The High-Resolution Rapid Refresh (HRRR): An hourly updating convection-
707 allowing forecast model. Part I: Motivation and system description. *Weather and*
708 *Forecasting*, 37(8), 1371-1395. <https://doi.org/10.1175/WAF-D-21-0151.1>
- 709 Duda, J. D., & Turner, D. D. (2021). Large-sample application of radar reflectivity object-based
710 verification to evaluate HRRR warm-season forecasts. *Weather and Forecasting*, 36(3),
711 805-821. <https://doi.org/10.1175/WAF-D-20-0203.1>
- 712 Duda, J. D., & Turner, D. D. (2023). Using object-based verification to assess improvements in
713 forecasts of convective storms between operational HRRR versions 3 and 4. *Weather and*
714 *Forecasting*, 38(10), 1971-1994. <https://doi.org/10.1175/WAF-D-22-0181.1>
- 715 Fan, J., Han, B., Varble, A., Morrison, H., North, K., Kollias, P., et al. (2017). Cloud-resolving
716 model intercomparison of an MC3E squall line case: Part I – Convective updrafts. *Journal*
717 *of Geophysical Research: Atmospheres*, 122(17), 9351-9378.
718 <https://doi.org/10.1002/2017JD026622>
- 719 Fairless, T., & Giangrande, S. (2018). *Interpolated sonde (INTERPOLATEDSONDE)*. ARM
720 User Facility, accessed 8 March 2021. <https://doi.org/10.5439/1095316>
- 721 Feng, Z., Leung, L. R., Houze, R. A., Hagos, S., Hardin, J., Yang, Q., et al. (2018). Structure and
722 evolution of mesoscale convective systems: Sensitivity to cloud microphysics in
723 convection-permitting simulations over the United States. *Journal of Advances in Modeling*
724 *Earth Systems*, 10(7), 1470-1494. <https://doi.org/10.1029/2018MS001305>
- 725 Feng, Z., Varble, A., Hardin, J., Marquis, J., Hunzinger, A., Zhang, Z., & Thieman, M. (2022).
726 Deep convection initiation, growth, and environments in the complex terrain of Central
727 Argentina during CACTI. *Monthly Weather Review*, 150(5), 1135-1155.
728 <https://doi.org/10.1175/mwr-d-21-0237.1>

- 729 Feng, Z., Hardin, J., Barnes, H. C., Li, J., Leung, L. R., Varble, A., & Zhang, Z. (2023a).
730 PyFLEXTRKR: a flexible feature tracking Python software for convective cloud analysis.
731 *Geoscientific Model Development*, 16(10), 2753-2776. [https://doi.org/10.5194/gmd-16-](https://doi.org/10.5194/gmd-16-2753-2023)
732 [2753-2023](https://doi.org/10.5194/gmd-16-2753-2023)
- 733 Feng, Z., Leung, L. R., Hardin, J., Terai, C. R., Song, F., & Caldwell, P. (2023b). Mesoscale
734 convective systems in DYAMOND global convection-permitting simulations. *Geophysical*
735 *Research Letters*, 50(4), e2022GL102603. <https://doi.org/10.1029/2022GL102603>
- 736 Gamache, J., & Houze, R. A. (1983). Water budget of a mesoscale convective system in the
737 tropics. *Journal of the Atmospheric Sciences*, 40(7), 1835-1850.
738 [https://doi.org/10.1175/1520-0469\(1983\)040<1835:WBOAMC>2.0.CO;2](https://doi.org/10.1175/1520-0469(1983)040<1835:WBOAMC>2.0.CO;2)
- 739 Giangrande, S. E., Collis, S., Theisen, A. K., & Tokay, A. (2014). Precipitation estimation from
740 the ARM distributed radar network during the MC3E campaign. *Journal of Applied*
741 *Meteorology and Climatology*, 53(9), 2130-2147. [https://doi.org/10.1175/JAMC-D-13-](https://doi.org/10.1175/JAMC-D-13-0321.1)
742 [0321.1](https://doi.org/10.1175/JAMC-D-13-0321.1)
- 743 Glenn, I. B., & Krueger, S. K. (2017). Connections matter: Updraft merging in organized tropical
744 deep convection. *Geophysical Research Letters*, 44(13), 7087-7094.
745 <https://doi.org/10.1002/2017GL074162>
- 746 Grim, J. A., Pinto, J. O., Blitz, T., Stone, K., & Dowell, D. C. (2021). Biases in the prediction of
747 convective storm characteristics with a convection allowing ensemble. *Weather and*
748 *Forecasting*, 37(1), 65-83. <https://doi.org/10.1175/WAF-D-21-0106.1>
- 749 Hagos, S., Feng, Z., Burleyson, C. D., Lim, K. S. S., Long, C. N., Wu, D., & Thompson, G.
750 (2014). Evaluation of convection-permitting model simulations of cloud populations
751 associated with the Madden-Julian oscillation using data collected during the
752 AMIE/DYNAMO field campaign. *Journal of Geophysical Research*, 119(21), 12,052-
753 12,068. <https://doi.org/10.1002/2014JD022143>
- 754 Han, B., Fan, J., Varble, A., Morrison, H., Williams, C. R., Chen, B., et al. (2019). Cloud-
755 resolving model intercomparison of an MC3E squall line case: Part II. Stratiform
756 precipitation properties. *Journal of Geophysical Research: Atmospheres*, 124(2), 1090-
757 1117. <https://doi.org/10.1029/2018JD029596>
- 758 Hardin, J., Hunzinger, A., Schuman, E., Matthews, A., Bharadwaj, N., Varble, A., et al. (2018).
759 *C-band scanning ARM precipitation radar, CF-radial, quality-controlled plan position*
760 *indicator scans (CSAPR2CFRPPIQC)*. ARM User Facility, accessed 9 March
761 2021. <https://doi.org/10.5439/1615604>
- 762 Hardin, J., Hunzinger, A., Schuman, E., Matthews, A., Bharadwaj, N., Varble, A., et al. (2020).
763 CACTI radar b1 processing: Corrections, calibrations, and processing report. *ARM*
764 *Technical Document DOE/SC-ARM-TR-244*, 46 pp.
- 765 Heistermann, M., Jacobi, S., & Pfaff, T. (2013). Technical Note: An open source library for
766 processing weather radar data (wradlib). *Hydrology and Earth System Sciences*, 17(2), 863-
767 871. <https://doi.org/10.5194/hess-17-863-2013>
- 768 Helmus, J. J., & Collis, S. M. (2016). The Python ARM Radar Toolkit (Py-ART), a library for
769 working with weather radar data in the Python programming language. *Journal of Open*
770 *Research Software*, 4(1), e25. <https://doi.org/10.5334/jors.119>
- 771 Houze, R. A. (2004). Mesoscale convective systems. *Reviews of Geophysics*, 42(4), RG4003.
772 <https://doi.org/10.1029/2004RG000150>
- 773 Iacono, M. J., Delamere, J. S., Mlawer, E. J., Shephard, M. W., Clough, S. A., & Collins, W. D.
774 (2008). Radiative forcing by long-lived greenhouse gases: Calculations with the AER

- 775 radiative transfer models. *Journal of Geophysical Research Atmospheres*, 113, D13103.
776 <https://doi.org/10.1029/2008JD009944>
- 777 Janjic, Z. (2002). Nonsingular Implementation of the Mellor-Yamada Level 2.5 Scheme in the
778 NCEP Meso model. *National Center for Environmental Prediction Office Note 437*, 61 pp.
- 779 Jeevanjee, N., & Zhou, L. (2022). On the resolution-dependence of anvil cloud fraction and
780 precipitation efficiency in radiative-convective equilibrium. *Journal of Advances in*
781 *Modeling Earth Systems*, 14(3), e2021MS002759. <https://doi.org/10.1029/2021MS002759>
- 782 Lakshmanan, V., Hondl, K., Potvin, C. K., & Preignitz, D. (2013). An improved method for
783 estimating radar echo-top height. *Weather and Forecasting*, 28(2), 481-488.
784 <https://doi.org/10.1175/WAF-D-12-00084.1>
- 785 Lebo, Z. J., & Morrison, H. (2015). Effects of horizontal and vertical grid spacing on mixing in
786 simulated squall lines and implications for convective strength and structure. *Monthly*
787 *Weather Review*, 143(11), 4355–4375. <https://doi.org/10.1175/MWR-D-15-0154.1>
- 788 Liu, C., Shige, S., Takayabu, Y. N., & Zipser, E. (2015). Latent heating contribution from
789 precipitation systems with different sizes, depths, and intensities in the tropics. *Journal of*
790 *Climate*, 28(1), 186-203. <https://doi.org/10.1175/JCLI-D-14-00370.1>
- 791 Lucas, C., Zipser, E. J., & LeMone, M. A. (1994). Vertical velocity in oceanic convection off
792 tropical Australia. *Journal of Atmospheric Sciences*, 51(21), 3183–3193.
793 [https://doi.org/10.1175/1520-0469\(1994\)051<3183:VVIOCO>2.0.CO;2](https://doi.org/10.1175/1520-0469(1994)051<3183:VVIOCO>2.0.CO;2)
- 794 Marquis, J. N., Feng, Z., Varble, A., Nelson, T. C., Houston, A., Peters, J. M., et al. (2023).
795 Near-cloud atmospheric ingredients for deep convection initiation. *Monthly Weather*
796 *Review*, 151(5), 2147-1267. <https://doi.org/10.1175/MWR-D-22-0243.1>
- 797 Marquis, J. N., Varble, A. C., Robinson, P., Nelson, T. C., & Friedrich, K. (2021). Low-level
798 mesoscale and cloud-scale interactions promoting deep convection initiation. *Monthly*
799 *Weather Review*, 149(8), 2473-2495. <https://doi.org/10.1175/MWR-D-20-0391.1>
- 800 Morrison, H., Morales, A., & Villanueva-Birriel, C. (2015). Concurrent sensitivities of an
801 idealized deep convective storm to parameterization of microphysics, horizontal grid
802 resolution, and environmental static stability. *Monthly Weather Review*, 143(6), 2082-2104.
803 <https://doi.org/10.1175/MWR-D-14-00271.1>
- 804 Morrison, H. (2016). Impacts of updraft size and dimensionality on the perturbation pressure and
805 vertical velocity in cumulus convection. Part II: Comparison of theoretical and numerical
806 solutions and fully dynamical simulations. *Journal of the Atmospheric Sciences*, 73(4),
807 1455-1480. <https://doi.org/10.1175/JAS-D-15-0041.1>
- 808 Mulholland, J. P., Nesbitt, S. W., Trapp, R. J., Rasmussen, K. L., & Salio, P. V. (2018).
809 Convective storm life cycle and environments near the Sierras de Córdoba, Argentina.
810 *Monthly Weather Review*, 146(8), 2541-2557. <https://doi.org/10.1175/MWR-D-18-0081.1>
- 811 Mulholland, J. P., Nesbitt, S. W., & Trapp, R. J. (2019). A case study of terrain influences on
812 upscale convective growth of a supercell. *Monthly Weather Review*, 147(12), 4305-4324.
813 <https://doi.org/10.1175/MWR-D-19-0099.1>
- 814 Nakanishi, M., & Niino, H. (2006). An improved Mellor-Yamada Level-3 model: Its numerical
815 stability and application to a regional prediction of advection fog. *Boundary-Layer*
816 *Meteorology*, 119, 397-407. <https://doi.org/10.1007/s10546-005-9030-8>
- 817 Nakanishi, M., & Niino, H. (2009). Development of an improved turbulence closure model for
818 the atmospheric boundary layer. *Journal of the Meteorological Society of Japan*, 87(5),
819 895-912. <https://doi.org/10.2151/jmsj.87.895>

- 820 Nelson, T. C., Marquis, J., Varble, A., & Friedrich, K. (2021). Radiosonde observations of
821 environments supporting deep moist convection initiation during RELAMPAGO-CACTI.
822 *Monthly Weather Review*, *149*(1), 289-309. <https://doi.org/10.1175/MWR-D-20-0148.1>
- 823 Nelson, T. C., Marquis, J., Peters, J. M., & Friedrich, K. (2022). Environmental controls on
824 simulated deep moist convection initiation occurring during RELAMPAGO-CACTI.
825 *Journal of the Atmospheric Sciences*, *79*(6), 1941-1964. <https://doi.org/10.1175/JAS-D-21-0226.1>
- 826
- 827 Nicol, J. C., Hogan, R. J., Stein, T. H. M., Hanley, K. E., Clark, P. A., Halliwell, C. E., et al.
828 (2015). Convective updraught evaluation in high resolution NWP simulations using single-
829 Doppler radar measurements. *Quarterly Journal of the Royal Meteorological Society*,
830 *141*(693), 3177-3189. <https://doi.org/10.1002/qj.2602>
- 831 Pan, D.-M., & Randall, D. D. A. (1998). A cumulus parameterization with a prognostic closure.
832 *Quarterly Journal of the Royal Meteorological Society*, *124*(547), 949-981.
833 <https://doi.org/10.1002/qj.49712454714>
- 834 Petch, J. C., Brown, A. R., & Gray, M. E. B. (2002). The impact of horizontal resolution on the
835 simulations of convective development over land. *Quarterly Journal of the Royal*
836 *Meteorological Society*, *128*(584), 2031-2044.
837 <https://doi.org/10.1256/003590002320603511>
- 838 Piersante, J. O., Rasmussen, K. L., Schumacher, R. S., Rowe, A. K., & McMurdie, L. A. (2021).
839 A Synoptic evolution comparison of the smallest and largest MCSs in subtropical South
840 America between spring and summer. *Monthly Weather Review*, *149*(6), 1943-1966.
841 <https://doi.org/10.1175/MWR-D-20-0208.1>
- 842 Prein, A. F., Gobiet, A., Suklitsch, M., Truhetz, H., Awan, N. K., Keuler, K., & Georgievski, G.
843 (2013). Added value of convection permitting seasonal simulations. *Climate Dynamics*, *41*,
844 2655–2677. <https://doi.org/10.1007/s00382-013-1744-6>
- 845 Prein, A. F., Liu, C., Ikeda, K., Bullock, R., Rasmussen, R. M., Holland, G. J., & Clark, M.
846 (2017). Simulating North American mesoscale convective systems with a convection-
847 permitting climate model. *Climate Dynamics*, *55*, 95-110. <https://doi.org/10.1007/s00382-017-3993-2>
- 848
- 849 Prein, A. F., Rasmussen, R. M., Wang, D., & Giangrande, S. (2021). Sensitivity of organized
850 convective storms to model grid spacing in current and future climates. *Philosophical*
851 *Transactions of the Royal Society A*, *379*(2195), 20190546.
852 <https://doi.org/10.1098/rsta.2019.0546>
- 853 Rasmussen, K. L., & Houze, R. A. (2011). Orographic convection in subtropical South America as
854 seen by the TRMM satellite. *Monthly Weather Review*, *139*(8), 2399-2420.
855 <https://doi.org/10.1175/MWR-D-10-05006.1>
- 856 Rasmussen, K. L., & Houze, R. A. (2016). Convective initiation near the Andes in subtropical
857 South America. *Monthly Weather Review*, *144*(6), 2351-2374.
858 <https://doi.org/10.1175/MWR-D-15-0058.1>
- 859 Ribeiro, B. Z., & Bosart, L. F. (2018). Elevated mixed layers and associated severe thunderstorm
860 environments in South and North America. *Monthly Weather Review*, *146*(1), 3-28.
861 <https://doi.org/10.1175/MWR-D-17-0121.1>
- 862 Rocque, M. N., & Rasmussen, K. L. (2022). The impact of topography on the environment and
863 life cycle of weakly and strongly forced MCSs during RELAMPAGO. *Monthly Weather*
864 *Review*, *150*(9), 2317-2338. <https://doi.org/10.1175/MWR-D-22-0049.1>

- 865 Rotunno, R., Klemp, J. B., & Weisman, M. L. (1988). A theory for strong, long-lived squall
866 lines. *Journal of the Atmospheric Sciences*, 45(3), 463-485. [https://doi.org/10.1175/1520-0469\(1988\)045<0463:ATFSSL>2.0.CO;2](https://doi.org/10.1175/1520-0469(1988)045<0463:ATFSSL>2.0.CO;2)
- 867
868 Salio, P., Nicolini, M., & Saulo, A. C. (2002). Chaco low-level jet events characterization during
869 the austral summer season. *Journal of Geophysical Research Atmospheres*, 107(D24), 4816.
870 <https://doi.org/10.1029/2001JD001315>
- 871 Salio, Paola, Nicolini, M., & Zipser, E. J. (2007). Mesoscale convective systems over
872 southeastern South America and their relationship with the South American Low-Level Jet.
873 *Monthly Weather Review*, 135(4), 1290-1309. <https://doi.org/10.1175/MWR3305.1>
- 874 Sasaki, C. R. S., Rowe, A. K., McMurdie, L. A., & Rasmussen, K. L. (2022). New Insights into
875 the South American Low-Level Jet from RELAMPAGO Observations. *Monthly Weather*
876 *Review*, 150(6), 1247-1271. <https://doi.org/10.1175/MWR-D-21-0161.1>
- 877 Sasaki, C. R. S., Rowe, A. K., McMurdie, L. A., Varble, A. C., & Zhang, Z. (2024). Influences
878 of the South American Low-Level Jet on the convective environment in central Argentina
879 using a convection-permitting simulation. *Monthly Weather Review*, 152(2), 629–648.
880 <https://doi.org/10.1175/MWR-D-23-0122.1>
- 881 Schumacher, C., Houze, R. A., & Kraucunas, I. (2004). The tropical dynamical response to latent
882 heating estimates derived from the TRMM Precipitation Radar. *Journal of the Atmospheric*
883 *Sciences*, 61(12), 1341–1358. [https://doi.org/10.1175/1520-0469\(2004\)061<1341:TTDRTL>2.0.CO;2](https://doi.org/10.1175/1520-0469(2004)061<1341:TTDRTL>2.0.CO;2)
- 884
885 Schumacher, R. S., Hence, D. A., Nesbitt, S. W., Trapp, R. J., Kosiba, K. A., Wurman, J., et al.
886 (2021). Convective-storm environments in subtropical South America from high-frequency
887 soundings during RELAMPAGO-CACTI. *Monthly Weather Review*, 149(5), 1439-1458.
888 <https://doi.org/10.1175/MWR-D-20-0293.1>
- 889 Seluchi, M. E., Saulo, A. C., Nicolini, M., & Satyamurty, P. (2003). The Northwestern
890 Argentinean Low: A study of two typical events. *Monthly Weather Review*, 131(10), 2361-
891 2378. [https://doi.org/10.1175/1520-0493\(2003\)131<2361:TNALAS>2.0.CO;2](https://doi.org/10.1175/1520-0493(2003)131<2361:TNALAS>2.0.CO;2)
- 892 Singh, I., Nesbitt, S. W., & Davis, C. A. (2022). Quasi-idealized numerical simulations of
893 processes involved in orogenic convection initiation over the Sierras de Córdoba. *Journal of*
894 *the Atmospheric Sciences*, 79(4), 1127-1149. <https://doi.org/10.1175/JAS-D-21-0007.1>
- 895 Skamarock, W. C., Klemp, J. B., Dudhia, J. Gill, D. O., Liu, Z., Berner, J., et al. (2019). A
896 Description of the Advanced Research WRF Model Version 4. *NCAR Technical Note*
897 *NCAR/TN-556+STR*.
- 898 Skamarock, William C. (2004). Evaluating mesoscale NWP models using kinetic energy spectra.
899 *Monthly Weather Review*, 132(12), 3019-3032. <https://doi.org/10.1175/MWR2830.1>
- 900 Stanford, M. W., Varble, A., Zipser, E., Strapp, J. W., Leroy, D., Schwarzenboeck, A., et al.
901 (2017). A ubiquitous ice size bias in simulations of tropical deep convection. *Atmospheric*
902 *Chemistry and Physics*, 17(15), 9599-9621. <https://doi.org/10.5194/acp-17-9599-2017>
- 903 Stanford, M. W., Morrison, H., & Varble, A. (2020). Impacts of stochastic mixing in idealized
904 convection-permitting simulations of squall lines. *Monthly Weather Review*, 148(12), 4971-
905 4994. <https://doi.org/10.1175/mwr-d-20-0135.1>
- 906 Stanford, M. W., Varble, A. C., & Morrison, H. (2024). Evaluation of a stochastic mixing
907 scheme in the deep convective gray zone using a tropical oceanic deep convection case
908 study. *Journal of Advances in Modeling Earth Systems*, 16(1), e2023MS003748.
909 <https://doi.org/10.1029/2023MS003748>

- 910 Stein, T. H. M., Hogan, R. J., Clark, P. A., Halliwell, C. E., Hanley, K. E., Lean, H. W., et al.
911 (2015). The DYMECS project: A Statistical approach for the evaluation of convective
912 storms in high-resolution NWP models. *Bulletin of the American Meteorological Society*,
913 *96*(6), 939-951. <https://doi.org/10.1175/BAMS-D-13-00279.1>
- 914 Steiner, M., Houze, R. A., & Yuter, S. E. (1995). Climatological characterization of three-
915 dimensional storm structure from operational radar and rain gauge data. *Journal of Applied*
916 *Meteorology*, *34*(9), 1978-2007. [https://doi.org/10.1175/1520-](https://doi.org/10.1175/1520-0450(1995)034<1978:CCOTDS>2.0.CO;2)
917 [0450\(1995\)034<1978:CCOTDS>2.0.CO;2](https://doi.org/10.1175/1520-0450(1995)034<1978:CCOTDS>2.0.CO;2)
- 918 Thompson, G., & Eidhammer, T. (2014). A study of aerosol impacts on clouds and precipitation
919 development in a large winter cyclone. *Journal of the Atmospheric Sciences*, *71*(10), 3636-
920 3658. <https://doi.org/10.1175/JAS-D-13-0305.1>
- 921 Trapp, R. J., Kosiba, K. A., Marquis, J. N., Kumjian, M. R., Nesbitt, S. W., Wurman, J., et al.
922 (2020). Multiple-platform and multiple-doppler radar observations of a supercell
923 thunderstorm in South America during RELAMPAGO. *Monthly Weather Review*, *148*(8),
924 3225-3241. <https://doi.org/10.1175/MWR-D-20-0125.1>
- 925 Varble, A., Fridlind, A. M., Zipser, E. J., Ackerman, A. S., Chaboureau, J. P., Fan, J., et al.
926 (2011). Evaluation of cloud-resolving model intercomparison simulations using TWP-ICE
927 observations: Precipitation and cloud structure. *Journal of Geophysical Research*
928 *Atmospheres*, *116*, D12206. <https://doi.org/10.1029/2010JD015180>
- 929 Varble, A., Zipser, E. J., Fridlind, A. M., Zhu, P., Ackerman, A. S., Chaboureau, J. P., Collis, S.,
930 et al. (2014a). Evaluation of cloud-resolving and limited area model intercomparison
931 simulations using TWP-ICE observations: 1. Deep convective updraft properties. *Journal of*
932 *Geophysical Research*, *119*(24), 13,891-13,918. <https://doi.org/10.1002/2013JD021371>
- 933 Varble, A., Zipser, E. J., Fridlind, A. M., Zhu, P., Ackerman, A. S., Chaboureau, J.-P., et al.
934 (2014b). Evaluation of cloud-resolving and limited area model intercomparison simulations
935 using TWP-ICE observations: 1. Precipitation microphysics. *Journal of Geophysical*
936 *Research: Atmospheres*, *119*(24), 13,919-13,945. <https://doi.org/10.1002/2013JD021372>
- 937 Varble, A., Morrison, H., & Zipser, E. (2020). Effects of Under-Resolved Convective Dynamics
938 on the Evolution of a Squall Line. *Monthly Weather Review*, *148*(1), 289–311.
939 <https://doi.org/10.1175/mwr-d-19-0187.1>
- 940 Varble, A. C., Nesbitt, S. W., Salio, P., Hardin, J. C., Bharadwaj, N., Borque, P., et al. (2021).
941 Utilizing a storm-generating hotspot to study convective cloud transitions: The CACTI
942 experiment. *Bulletin of the American Meteorological Society*, *102*(8), E1597-E1620.
943 <https://doi.org/10.1175/BAMS-D-20-0030.1>
- 944 Vera, C., Baez, J., Douglas, M., Emmanuel, C. B., Marengo, J., Meitin, J., et al. (2006). The
945 South American Low-Level Jet experiment. *Bulletin of the American Meteorological*
946 *Society*, *87*(1), 63-78. <https://doi.org/10.1175/BAMS-87-1-63>
- 947 Wang, D., Giangrande, S. E., Feng, Z., Hardin, J. C., & Prein, A. F. (2020). Updraft and
948 Downdraft Core Size and Intensity as Revealed by Radar Wind Profilers: MCS
949 Observations and Idealized Model Comparisons. *Journal of Geophysical Research:*
950 *Atmospheres*, *125*(11), e2019JD031774. <https://doi.org/10.1029/2019JD031774>
- 951 Wang, D., Prein, A. F., Giangrande, S. E., Ramos-Valle, A., Ge, M., & Jensen, M. P. (2022).
952 Convective Updraft and Downdraft Characteristics of Continental Mesoscale Convective
953 Systems in the Model Gray Zone. *Journal of Geophysical Research: Atmospheres*, *127*(16),
954 e2022JD036746. <https://doi.org/10.1029/2022JD036746>

- 955 Warner, C., & McNamara, D. P. (1984). Aircraft measurements of convective draft cores in
956 MONEX. *Journal of the Atmospheric Sciences*, *41*(3), 430-438.
957 [https://doi.org/10.1175/1520-0469\(1984\)041<0430:AMOCDC>2.0.CO;2](https://doi.org/10.1175/1520-0469(1984)041<0430:AMOCDC>2.0.CO;2)
- 958 Yang, B., Qian, Y., Lin, G., Leung, L. R., Rasch, P. J., Zhang, G. J., et al. (2013). Uncertainty
959 quantification and parameter tuning in the CAM5 Zhang-McFarlane convection scheme and
960 impact of improved convection on the global circulation and climate. *Journal of*
961 *Geophysical Research Atmospheres*, *118*(2), 395-415.
962 <https://doi.org/10.1029/2012JD018213>
- 963 Yang, G.-Y., & Slingo, J. (2001). The diurnal cycle in the tropics. *Monthly Weather Review*,
964 *129*(4), 784–801. [https://doi.org/10.1175/1520-0493\(2001\)129<0784:TDCITT>2.0.CO;2](https://doi.org/10.1175/1520-0493(2001)129<0784:TDCITT>2.0.CO;2)
- 965 Yun, Y., Liu, C., Luo, Y., Liang, X., Huang, L., Chen, F., & Rasmussen, R. (2020). Convection-
966 permitting regional climate simulation of warm-season precipitation over Eastern China.
967 *Climate Dynamics*, *54*, 1469-1489. <https://doi.org/10.1007/s00382-019-05070-y>
- 968 Zhang, Z., Varble, A., Feng, Z., Hardin, J., & Zipser, E. (2021). Growth of Mesoscale
969 Convective Systems in Observations and a Seasonal Convection-Permitting Simulation over
970 Argentina. *Monthly Weather Review*, *149*(10), 3469-3490. [https://doi.org/10.1175/mwr-d-](https://doi.org/10.1175/mwr-d-20-0411.1)
971 [20-0411.1](https://doi.org/10.1175/mwr-d-20-0411.1)
- 972 Zhang, Z., Varble, A., & Feng, Z. (2024). Datasets for the Publication "Simulated Convective
973 Cell and System Growth Bias Dependencies on Atmospheric Instability and Model
974 Resolution" [Dataset]. Zenodo. <https://doi.org/10.5281/zenodo.10655168>
975